AAlborg University

Master Thesis

Glioblastoma and the Blood–Brain Barrier:
Insights into Barrier Integrity and Tumour–Endothelial Interactions

Author: Stefan Holmgård Jespersen

August 15, 2025

Department of Health Science and Technology
The Faculty of Medicine
Medicine with Industrial Specialisation
Biomedicine
https://www.hst.aau.dk

Title:

Glioblastoma and the Blood–Brain Barrier: Insights into Barrier Integrity and Tumour–Endothelial Interactions

Project:

Glioblastoma and the Blood-Brain Barrier

Project Period:

September 1st 2024 - August 15th 2025

Project Group:

9021

Participants:

Stefan Holmgård Jespersen

Supervisor:

Louiza Bohn Thomsen, Ph.D., Associate Professor

Project Technicians:

Ditte Bech Laursen and Merete Fredsgaard

Number of Pages: 40 pages
Appendix: 6 pages
Date of Completion: August 12th 2025

1 Abstract

Glioblastoma (GBM) is the most aggressive primary brain tumour, characterised by profound resistance to therapy. A significant barrier to effective treatment is the blood–brain barrier (BBB) and its pathological variant, the blood–brain tumour barrier (BBTB), which can limit drug penetration. While GBM is often assumed to disrupt BBB integrity, the present study used primary porcine brain capillary endothelial cells (PBCECs) in co-culture with glioblastoma cell lines to test this paradigm. Co-cultures were established with either the long-established Human U87 GBM-associated cell line, the low-passage patient-derived T10 GBM-associated cell line, or primary porcine astrocytes as a non-malignant reference. The barrier function was assessed via transendothelial electrical resistance (TEER), and the expression of Claudin-5, ZO-1, MFSD2A, and CD93 was quantified at both the mRNA and protein levels. Pharmacological inhibition of MFSD2A (tunicamycin) and CD93 (metoclopramide) was employed to investigate the mechanistic contributions.

Across a 9-day co-culture period, PBCEC & T10 displayed the most significant barrier reinforcement, with TEER and Claudin-5 expression markedly exceeding those of U87 and astrocyte co-cultures. This effect persisted despite single-target inhibition of MFSD2A or CD93, suggesting redundancy in glioblastoma-derived pro-barrier signals. Discrepancies between mRNA and protein responses to metoclopramide indicate possible post-transcriptional regulation or biological variation between inserts. The modest reinforcement by astrocytes supports a glioblastoma-specific effect.

These findings challenge the view that GBM universally compromises BBB integrity and highlight the context-dependent nature of tumour–endothelial interactions. From a translational perspective, reinforced BBTB function may contribute to therapeutic resistance, underscoring the need for strategies enabling transient, controlled barrier modulation to improve drug delivery without long-term compromise of BBB function.

2 Preface

This thesis was conducted as part of the Master's programme in Medicine with Industrial Specialisation (Biomedicine) at Aalborg University. The work was conducted out at the Department of Health Science and Technology from September 1, 2024, to August 15, 2025.

My academic interest in neuroscience, combined with a growing awareness of glioblastoma's complexity and impact, formed the basis for choosing this topic. Glioblastoma's aggressive nature and the challenges it presents within neuro-oncology have made it a subject of both scientific and personal importance to me, having experienced the loss of people close to me to this disease.

The primary objective of this project was not only to investigate the interplay between glioblastoma and the blood–brain barrier but also to gain experience in independently planning, executing, and managing a large, multi-semester research project under supervision. The process has provided valuable insight into both the scientific and practical aspects of research in an academic setting.

3 Acknowledgements

First and foremost, I would like to thank my supervisor, Louiza Bohn Thomsen, for invaluable guidance, encouragement, and constructive feedback throughout this project. Your support in both the laboratory and the writing process has been essential, and I am grateful for your patience and willingness to share your knowledge.

I also wish to thank the laboratory technicians — Merete Fredsgaard, Hanne Krone Nielsen, Ditte Bech Laursen, and Brita Holst Serup — for their technical expertise and assistance with the experimental work. Your help in the laboratory made a real difference in motivating me and keeping the project on track.

I am grateful to the Medical Microbiology and Immunology group for providing a collaborative and supportive research environment. Special thanks go to Trine Søndergaard Jensen and Natasja Bruun for the comforting and inspiring coffee talks.

A special thanks to Thomas and Lene from Sæby Gaardslagteri I/S for providing the porcine brains used in this project.

Finally, I would like to thank my classmates Julie R. Nielsen, Emma G. Larsen, Signe Dissing Hansen, Trine Kjær Lauritzen, Sophie Fromholt, Kathrine Overgaard Jensen, Line Jørgensen, Marco Peters, and Mikkel Skov. Working alongside you has made this year both rewarding and enjoyable.

Contents

4 Introduction

Cancer is a major global health problem and one of the leading causes of death, with 9.7 million deaths worldwide in 2022 [Bray et al., 2024], while in Denmark, 26.5% of all deaths in 2022 were attributed to cancer [Danmarks-Statistik, 2024]. It is the most common cause of death, with 49.2% higher mortality than heart disease [Danmarks-Statistik, 2024].

CNS tumours are the most common solid tumours and the leading cause of cancer-related death in individuals aged 0–19 [Schaff and Mellinghoff, 2023]. While particularly devastating in children and adolescents, these tumours also represent a significant health burden in adults. Each year, approximately 85,000 people in the U.S. are diagnosed with a primary brain tumour, with about 29% classified as malignant [Ostrom et al., 2022].

4.1 Glioblastoma

Glioblastoma (GBM) is an adult-type diffuse glioma, along with astrocytoma and oligodendrocytoma [Louis et al., 2021]. GBM is one of the most common primary malignancies in the CNS, representing 48.6% of all cases [Grochans et al., 2022], and is more prevalent in men compared to women [Grochans et al., 2022]. In Denmark, the male incidence rate is 1.62 times that of females, with a median age of 66 years [Hansen et al., 2018]. In the CNS, tumours are classified from grade 1 to 4 by the World Health Organisation (WHO) according to prognosis [Louis et al., 2021, Torp et al., 2022]. GBM is classified as a grade 4 tumour, indicating its rapid growth and poor prognosis [Louis et al., 2021], the median overall survival for patients with GBM in Denmark was only 11.2 months [Hansen et al., 2018].

GBM is a highly aggressive and malignant brain tumour [Loras et al., 2023, Beiriger et al., 2022], and the origin of GBM is still unclear. The two leading theories are that GBM originates from neural stem/precursor cells, such as astrocyte precursor cells and oligodendrocyte precursor cells or that GBM originates from astrocytes. [Loras et al., 2023, Beiriger et al., 2022].

Definition and General Characteristics of GBM

According to the 2021 WHO Classification of Tumours of the Central Nervous System, glioblastoma (GBM) is categorised under *adult-type diffuse gliomas* and is defined as a **CNS WHO Grade 4** tumour Verdugo et al. [2022], Louis et al. [2021]. The classification emphasises molecular features over purely histological criteria Louis et al. [2021]. GBM is defined explicitly as a diffuse astrocytic glioma that is *IDH-wildtype*, and must exhibit at least one of the following: *TERT* promoter mutation, *EGFR* amplification, or combined gain of chromosome 7 and loss of chromosome 10 Verdugo et al. [2022], Louis et al. [2021].

Transcriptomic profiling has revealed three major subtypes of IDH-wildtype GBM: **proneural**, **classical**, and **mesenchymal** Verdugo et al. [2022], Wang et al. [2017], Verhaak et al. [2010]. These subtypes are associated with distinct genetic and microenvironmental features Verdugo et al. [2022], Wang et al. [2017], Verhaak et al. [2010]. The proneural subtype is often linked to alterations in *PDGFRA*, *OLIG2*, and *TP53*; the classical subtype

is characterised by *EGFR* amplification and *TP53* mutations; and the mesenchymal subtype is associated with *NF1* loss and increased infiltration of tumour-associated macrophages Verdugo et al. [2022], Wang et al. [2017], Verhaak et al. [2010]. Importantly, these subtypes are not static. Longitudinal transcriptomic studies have demonstrated that GBM tumours can change subtypes over time, especially after treatment. Among the three, the **mesenchymal subtype is the most stable**, with 65% of tumours retaining this classification upon recurrence, compared to 51% for classical and 41% for proneural subtypes Wang et al. [2017].

Beyond classification, glioblastoma is defined by a set of interconnected biological processes/**hallmarks** that drive its malignancy and therapeutic resistance. These include:

1. **Selective advantages of growth and proliferation**: GBM cells exhibit deregulated signalling pathways such as Ras-Raf-MEK-ERK and PI3K/Akt/mTOR, promoting uncontrolled proliferation and survival Torrisi et al. [2022].

2. **Altered stress response**: GBM adapts to hypoxia and oxidative stress through mechanisms like HIF-1α activation, enhanced DNA repair, and autophagy, contributing to resistance against radiotherapy and chemotherapy Torrisi et al. [2022].

3. **Sustained vascularisation**: GBM maintains vascular support through multiple mechanisms, including angiogenesis, vascular mimicry, and glioma-to-endothelial transdifferentiation, despite the presence of hypoxic and necrotic regions Torrisi et al. [2022].

4. **Tissue invasion and metastasis**: GBM is highly invasive within the brain parenchyma, driven by epithelial-mesenchymal transition (EMT), cytoskeletal remodelling, and extracellular matrix degradation Torrisi et al. [2022].

5. **Metabolic rewiring**: GBM cells undergo metabolic shifts such as increased glycolysis, lipid accumulation, and glutaminolysis, enabling survival in nutrient-deprived and hypoxic environments Verdugo et al. [2022].

6. **Immune modulation**: GBM creates an immunosuppressive microenvironment by recruiting M2-like macrophages, inhibiting T-cell responses, and expressing immune checkpoint molecules such as PD-L1 Wang et al. [2017].

7. **Tumour microenvironment (TME) promotion**: These hallmarks converge to shape a supportive and protective TME, where glioma stem cells interact with immune cells, vasculature, and stromal components to sustain tumour growth and resistance Torrisi et al. [2022].

Current treatment options

The traditional treatment strategies for GBM are surgical resection, radiotherapy and chemotherapy, but they remain ineffective, evidenced by a 5-year survival of less than 10% [Wen et al., 2020, Rong et al., 2022]. Although a positive correlation between the degree of tumour resection and survival time, the infiltrative nature of GBM

prohibits a complete surgical resection of the tumour [Wu et al., 2021, Davis, 2016, Wen et al., 2020]. Because surgical resection is not curative alone, the primary goal is to prevent permanent neurological deficits rather than expanding the resection area [Wu et al., 2021, Davis, 2016, Wen et al., 2020]. Following surgical resection, radiotherapy targets the residual tumour cells by ionising the DNA, causing it to break, leading to cell death [Wu et al., 2021, Davis, 2016, Wen et al., 2020].radiotherapy is often used in combination with chemotherapy because patients who received radiotherapy and chemotherapy had a median OS of 14.6 months compared to 12.1 months for patients who only received radiotherapy [Stupp et al., 2005, Wu et al., 2021, Davis, 2016, Wen et al., 2020]. The chemotherapy of choice is Temozolomide due to its ability to cross the blood-brain barrier (BBB). Temozolomide works by damaging the cell's DNA by methylating guanine bases, and may lead to cell death [Wesolowski et al., 2010, Wu et al., 2021, Davis, 2016, Wen et al., 2020]. Although radiotherapy and chemotherapy prolong the median OS, the prognosis remains poor due to GBM's ability to resist these treatments [Chédeville and Madureira, 2021, Wesolowski et al., 2010, Wu et al., 2021, Davis, 2016, Wen et al., 2020]. It has been speculated that GBM might use hypoxia as a means of resistance to radiotherapy.

4.2 Blood-Brain Barrier

The blood-brain barrier is a highly specialised protective membrane formed by microvascular endothelial cells lining the cerebral capillaries in the central nervous system [Kadry et al., 2020, Lochhead et al., 2020]. It serves as the primary barrier separating the brain from the circulating blood [Kadry et al., 2020, Lochhead et al., 2020]. The BBB plays a critical role in maintaining brain homeostasis by controlling the influx and efflux of substances between the blood and the brain [Kadry et al., 2020]. It protects the CNS from potentially harmful circulating substances, including toxins and pathogens, while allowing the selective uptake of essential nutrients [Kadry et al., 2020, Lochhead et al., 2020]. In addition to protecting the brain from undesired agents, it also hinders the entry of desired agents, such as the drugs required for treatment. Only small lipophilic molecules with less than six hydrogen bonds and a molecular weight (MW) $\succ$ 400 Da can passively diffuse the barrier [Kadry et al., 2020]. To further complicate the delivery of drugs, the BBB exhibits high expression of P-glycoprotein (P-gp) and Breast Cancer Resistance Protein (BCRP). P-gp and BCRP are ATP-driven efflux transporters responsible for expelling substrates, including toxins and pharmaceutical medications, from the endothelial vessel wall into the bloodstream.

The functional and structural foundation of the blood-brain barrier (BBB) is constituted by the neurovascular unit (NVU) [Kugler et al., 2021, McConnell and Mishra, 2022]. The NVU represents a complex multicellular assembly comprising various essential components that collaboratively regulate cerebral blood flow, maintain the integrity of the BBB, and govern the transfer of substances between the bloodstream and the brain [Kugler et al., 2021, McConnell and Mishra, 2022].

Cells of the NVU

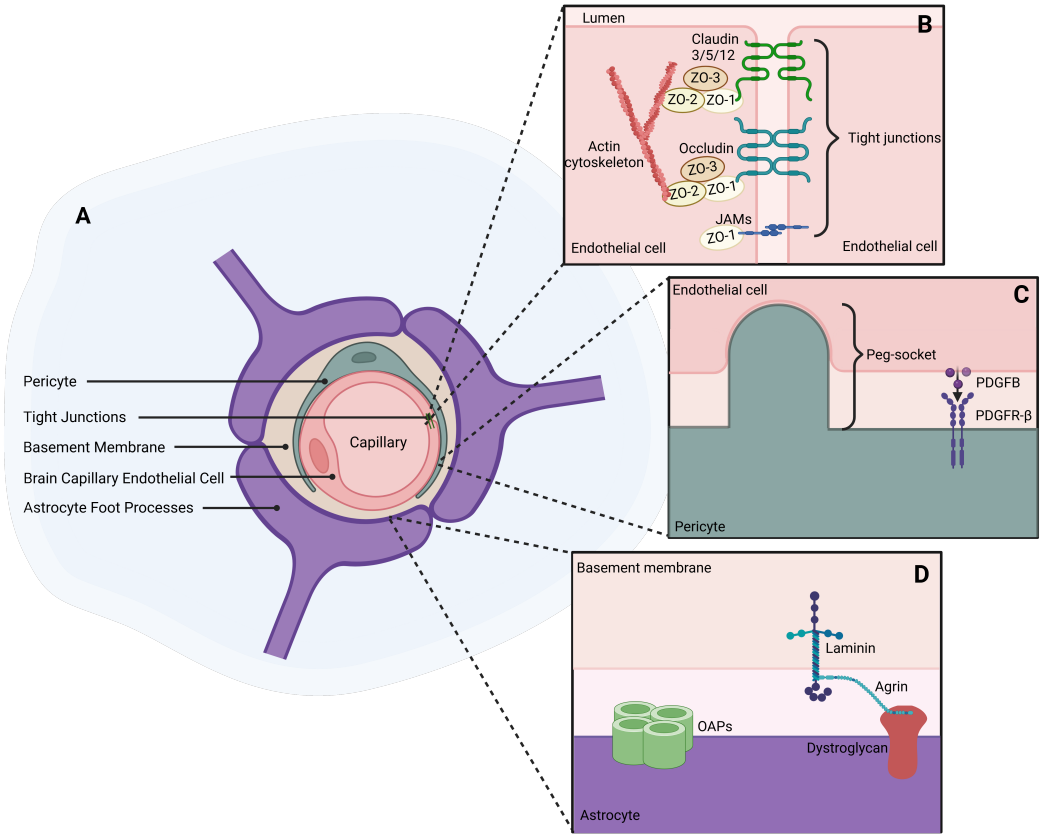

Figure 1: Overview of the neurovascular unit (NVU), highlighting some of the key cellular and molecular components involved in blood-brain barrier function. **(A)** Cross-sectional view of a brain capillary illustrating endothelial cells, pericytes, astrocyte endfeet, tight junctions, and the basement membrane. **(B)** Magnified view of endothelial cell–cell junctions showing tight junction proteins (claudins, occludin, junctional adhesion molecules) linked to the actin cytoskeleton via ZO proteins. **(C)** Endothelial–pericyte interaction through the peg–socket junction, mediated by platelet-derived growth factor-β (PDGFβ) and its receptor PDGFRβ. **(D)** Astrocyte–basement membrane interface, highlighting connections mediated by laminin, agrin, dystroglycan, and orthogonal arrays of particles (OAPs). Inspired by [Kadry et al., 2020, Wu et al., 2023, Abbott et al., 2010]). Created in BioRender.com.

Endothelial cells: Endothelial cells (ECs) are the central cellular component of the blood-brain barrier (BBB), and their specialised structural features are critical for maintaining its restrictive properties and regulating molecular exchange between the blood and the central nervous system (CNS) [Kadry et al., 2020, Wu et al., 2023]. The morphology of the ECs of the BBB is characterised by a flat appearance and having both the expression of tight junctions (TJ) and adherens junctions (AJ) that tightly seal the ECs (Figure.1B), limiting the paracellular diffusion of hydrophilic molecules [Abbott et al., 2010, Kadry et al., 2020, Wu et al., 2023]. The expression of TJs fences the luminal part of the EC from the basolateral region [Kadry et al., 2020, Wu et al., 2023]. The ECs of the BBB lack fenestrations, which enables them to tightly control the movement of molecules between the

bloodstream and brain tissue [Alhadidi et al., 2017, Wu et al., 2023]. Another characteristic of the EC of the BBB compared to peripheral ECs is the large number of mitochondria; thus, more energy is required for transport [Wu et al., 2023]. The functional characteristics of BBB ECs are that, because of the limited passive diffusion of hydrophilic molecules, they display specific transporters that allow the passage of water-soluble molecules essential for nervous tissue [Abbott et al., 2010, Wu et al., 2023]. Furthermore, they exhibit low expression of leukocyte adhesion molecules, which limits immune cell access [Wu et al., 2023].

Pericytes: Pericytes are mural cells and another integral part of the NVU, and they are embedded within the basement membrane, which they share with ECs [Kadry et al., 2020, Wu et al., 2023]. Pericytes cover the ECs in the CNS vasculature in a ratio of 1:1-1:3 and are considered the vasculature covered by the most pericytes in the body [Armulik et al., 2011, Kadry et al., 2020]. They form peg-socket type contacts with ECs (Figure.1C) where they insert small cytoplasmic fingers into the sockets in the ECs [Armulik et al., 2011]. The anatomical proximity between pericytes and endothelial cells allows for close signalling. It is observed, for example, in angiogenic endothelial cells, where the recruitment of pericytes is facilitated by the secretion of PDGF-B, which binds to PDGFRβ on the surface of developing pericytes [Armulik et al., 2011]. Another example of their interaction showed that the loss of pericytes leads to more permeable ECs by a reduced expression of TJs and AJ, indicating that pericytes perform an essential role in the structural preservation of the BBB. [Winkler et al., 2012, Armulik et al., 2010, Daneman et al., 2010].

Astrocytes: Astrocytes are a specialised glial cell and are the most abundant cell type in the CNS Allen and Eroglu [2017], Banker [1980], Sofroniew and Vinters [2009]. Astrocytes are divided into protoplasmatic and fibrous Sofroniew and Vinters [2009], Allen and Eroglu [2017]. Protoplasmatic astrocytes are in grey matter, while fibrous astrocytes are in white matter Sofroniew and Vinters [2009], Allen and Eroglu [2017]. They form an envelope around the cerebral capillaries, with their foot processes (Figure.1A) anchoring them to the perivascular basement membrane (Figure.1D) Abbott et al. [2006a], Wolburg-Buchholz et al. [2009]. These astrocytic endfeet are enriched with aquaporin-4 and Kir4.1 channels, which are organised into orthogonal arrays of particles (OAPs) and are essential for supporting barrier function by regulating perivascular ion and water balance Abbott et al. [2006a], Wolburg et al. [2011], Schiera et al. [2024]. In addition to fluid and ion homeostasis, astrocytes also participate in the regulation of cerebral blood flow by secreting prostaglandins and arachidonic acid, constricting or dilating the vessel lumen Sofroniew and Vinters [2009], Gordon et al. [2007], Mishra [2016]. Beyond their homeostatic functions, astrocytes play a crucial role in the development and maintenance of endothelial barrier properties. They interact with endothelial cells both through direct contact and by secreting soluble factors, including VEGF, TGF-β, and Wnt ligands, which modulate tight junction protein expression and endothelial phenotype Abbott et al. [2006a], Michinaga and Koyama [2019], Schiera et al. [2024]. Moreover, astrocyte-derived extracellular vesicles have been shown to carry bioactive molecules that affect endothelial gene expression and contribute to the regulation of barrier integrity Schiera et al. [2024].

Tight and Adherens Junctions

Claudins: Claudins are a family of TJ proteins with approximately 27 members and are located in the cell membrane in various types of cells [Tsukita et al., 2019, Tikiyani and Babu, 2019]. They have four transmembrane domains with two extracellular loops and intracellular N- and C-termini. Claudins are anchored to the cytoskeleton in cells through their C-terminal [Tsukita et al., 2019, Tikiyani and Babu, 2019, Kadry et al., 2020]. In the brain, the main expressions of claudin in ECs are claudins 3 and 5, and especially claudin-5 is the key TJ component in the tight paracellular barrier function of the BBB [Tsukita et al., 2019, Tikiyani and Babu, 2019, Kadry et al., 2020, Luissint et al., 2012]. Claudin-5 (Figure.1B) has a molecular weight of 23 kDa and is located in the apical part of ECs, where it binds to another Claudin-5 in adjacent ECs [Tsukita et al., 2019, Tikiyani and Babu, 2019, Kadry et al., 2020, Luissint et al., 2012]. Claudin-5 knockdowns in mice have been shown to compromise the BBB, causing leaky vessels and inducing brain inflammation [Nitta et al., 2003, Menard et al., 2017].

Occludin: Occludin (like claudins) is a transmembrane TJ protein similar to claudins, expressed in various types of cells. Still, it is highly expressed in neural EC compared to EC in other tissues [Kadry et al., 2020, Cardoso et al., 2010]. Occludin (Figure.1B) with its molecular weight of 65 kDa is much larger than claudins but also has four transmembrane domains in the apical part of the cell and binds to occludins in neighbouring ECs [Kadry et al., 2020, Cardoso et al., 2010, Lochhead et al., 2020]. High expressions of occludin have been shown to increase the paracellular barrier function of cerebral ECs [Lochhead et al., 2020, Cardoso et al., 2010]; however, mice with genetic knockdown of occludin have been shown to retain normal barrier functions [Sweeney et al., 2018, Hawkins and Davis, 2005, Luissint et al., 2012, Cardoso et al., 2010]. This suggests that compensatory mechanisms balance the loss of occludin and that it may not be essential to form an intact and functional BBB [Sweeney et al., 2018, Hawkins and Davis, 2005, Luissint et al., 2012, Cardoso et al., 2010].

Junctional Adhesion Molecules: Junctional Adhesion Molecules (JAM) are also a family of transmembranous TJ proteins with three members, JAM-1 to 3. They have a molecular weight of 40 kDa [Kadry et al., 2020, Cardoso et al., 2010, Lochhead et al., 2020]. JAMS (Figure.1B) have only a single transmembrane domain with a short intracellular C-terminal and an extracellular immunoglobulin-like domain that mediates binding to other JAMS in adjacent cells [Kadry et al., 2020, Cardoso et al., 2010, Lochhead et al., 2020]. Only JAM-1 and JAM-3 are found in the cerebral vasculature, whereas JAM-1 is mainly expressed in neural ECs, and JAM-3 is expressed in most ECs [Kadry et al., 2020, Cardoso et al., 2010, Lochhead et al., 2020].

Cytoplasmic accessory proteins: Cytoplasmic accessory proteins are intracellular TJ proteins that are essential for structural support, binding transmembranous TJ to the actin cytoskeleton [Kadry et al., 2020, Luissint et al., 2012, Lochhead et al., 2020]. The most notable cytoplasmic proteins are the membrane-associated guanylate kinase (MAGUK) family Zonula Occludens (ZO) 1 to 3 [Kadry et al., 2020, Luissint et al., 2012, Lochhead et al., 2020]. ZO-1 is the largest with a molecular weight of 225 kDa and together with ZO-2 (Figure.1B) is considered essential for the polymerisation of TJ [Kadry et al., 2020, Luissint et al., 2012, Lochhead et al., 2020,

Piontek et al., 2020, Umeda et al., 2006]. The structure of ZO proteins is made up of multiple domains for protein interaction: three PDZ domains, a guanyl kinase (GuK) domain, a Src homology 3 domain (SH3), and an actin binding domain [Kadry et al., 2020, Luissint et al., 2012, Lochhead et al., 2020, Piontek et al., 2020, Kuo et al., 2022]. These domains enable ZO-1 to bind to Claudins, Occludin, and JAM-1, thereby anchoring them to the actin cytoskeleton [Kadry et al., 2020, Luissint et al., 2012, Lochhead et al., 2020, Piontek et al., 2020, Kuo et al., 2022, Umeda et al., 2006].

Adherens Junctions: Adherens Junctions (AJs) are, as the name suggests, adhesion molecules and are located at the basolateral portion of the cell where they form homophilic contacts with neighbouring cells [Kadry et al., 2020, Cardoso et al., 2010, Stamatovic et al., 2016]. AJs contain transmembrane proteins, such as cadherins, and cytoplasmic proteins such as catenins [Kadry et al., 2020, Cardoso et al., 2010, Stamatovic et al., 2016]. In the BBB, the main transmembrane protein is VE-cadherin, where it's connected to the actin cytoskeleton through β and α-catenins [Kadry et al., 2020, Cardoso et al., 2010, Stamatovic et al., 2016].

4.3 Blood-Brain Tumour Barrier

The blood-brain tumour barrier (BBTB) (Figure 2) is a pathological derivative of the BBB that arises in the context of glioblastoma and other diffuse gliomas Watkins et al. [2014], van Tellingen et al. [2015]. The BBB is a tightly regulated interface that restricts the passage of molecules from the bloodstream into the brain parenchyma Arvanitis et al. [2020], Sarkaria et al. [2017]. In contrast, the BBTB exhibits a heterogeneous permeability profile, which varies across different regions of the tumour Arvanitis et al. [2020], Sarkaria et al. [2017].

Glioblastoma is spatially and pathologically heterogeneous, and this is reflected in the organisation of the BBTB Steeg [2021]. The **tumour core** is typically characterised by extensive barrier disruption, abnormal angiogenesis, and high metabolic activity Watkins et al. [2014], Steeg [2021]. In this region, the BBTB is severely compromised, allowing macromolecular leakage and extravasation of plasma proteins van Tellingen et al. [2015].

Surrounding the core are **infiltrative regions**, which extend into otherwise healthy brain tissue and contain migrating glioma cells Arvanitis et al. [2020]. These areas retain more BBB-like properties, including relatively preserved astrocytic organisation and reduced permeability Steeg [2021].

Moreover, glioblastoma is embedded within a dynamic and immunosuppressive **tumour microenvironment**, which includes reactive astrocytes, microglia, infiltrating immune cells, and stromal components Steeg [2021]. This microenvironment contributes to vascular remodelling, basement membrane alterations, and further barrier dysfunction Steeg [2021].

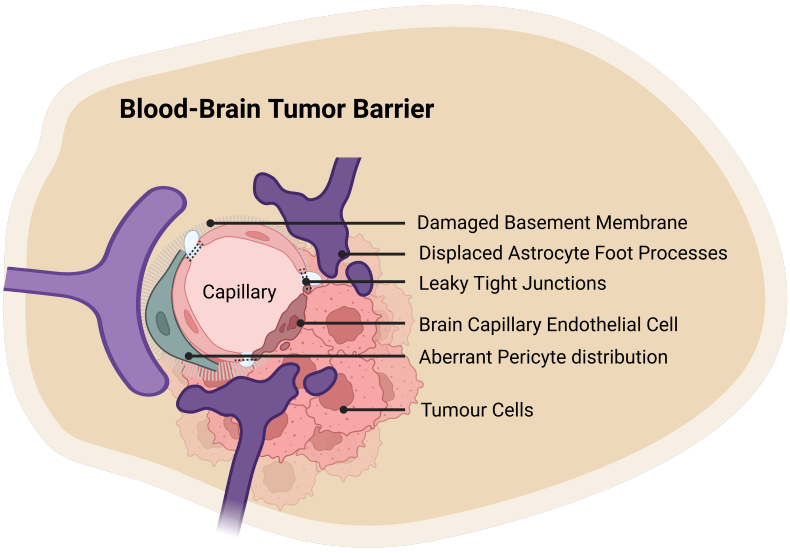

Figure 2: Illustration of the blood-brain tumour barrier (BBTB) in glioblastoma. The figure depicts key cellular components of the neurovascular unit. It highlights structural changes in the tumour vasculature, including disrupted tight junctions, damaged basement membrane, aberrant distribution of pericytes, and the displacement of astrocytes. Inspired by [Arvanitis et al., 2020, Steeg, 2021, Sarkaria et al., 2017]). Created in BioRender.com.

Endothelial Cells Of The BBTB: ECs of the BBTB undergo extensive structural and molecular remodelling in glioblastoma, resulting in a spatially heterogeneous barrier that complicates therapeutic delivery van Tellingen et al. [2015], Sarkaria et al. [2017], Arvanitis et al. [2020]. In the tumour core, ECs often display fenestrations, inter-endothelial gaps, and increased vesicular transport, contributing to a leaky vasculature van Tellingen et al. [2015], Arvanitis et al. [2020]. In contrast, infiltrative regions retain BBB-like ECs with continuous morphology and active efflux mechanisms, maintaining a restrictive phenotype Sarkaria et al. [2017], Arvanitis et al. [2020].

A central feature of BBTB dysfunction is the downregulation of tight junction proteins. Claudin-5 expression is significantly reduced in vessels contacted by glioma cells, while remaining abundant in glioma-free regions Watkins et al. [2014], van Tellingen et al. [2015], Arvanitis et al. [2020]. Quantitative analysis revealed a marked decrease in claudin-5 coverage in tumour-associated vessels, correlating with increased paracellular permeability Watkins et al. [2014]. Occludin levels are similarly diminished in glioma-infiltrated vasculature, contributing to the loss of endothelial sealing capacity Steeg [2021], Sarkaria et al. [2017].

These changes are compounded by the reduction of cytoplasmic accessory proteins such as ZO-1, which anchor transmembrane junctional proteins to the actin cytoskeleton Watkins et al. [2014], Arvanitis et al. [2020]. ZO-1 expression is notably reduced in regions where astrocytic endfeet have been displaced, further destabilising tight

junction architecture and facilitating macromolecular leakage Watkins et al. [2014], Arvanitis et al. [2020].

Junctional adhesion molecules (JAMs), which stabilise inter-endothelial contacts and regulate leukocyte trafficking, are also dysregulated in the BBTB. Upregulation of ICAM1 and JAMs has been observed in glioblastoma, promoting lymphocyte ingress and further destabilising the endothelial barrier Steeg [2021], Arvanitis et al. [2020], Sarkaria et al. [2017].

Adherens junctions are similarly compromised. VE-cadherin expression is downregulated in response to tumour-derived cytokines, including TNF-α and IL-6, weakening cell-cell adhesion and increasing vascular permeability Steeg [2021], Arvanitis et al. [2020]. These alterations are most pronounced in enhancing regions of glioblastoma, where vascular remodelling is active Sarkaria et al. [2017], van Tellingen et al. [2015].

Together, these endothelial changes spanning tight junctions, adhesion molecules, cytoskeletal linkers, and cadherin complexes reflect a multifaceted breakdown of BBTB integrity that facilitates tumour progression and immune cell infiltrationWatkins et al. [2014], van Tellingen et al. [2015], Steeg [2021], Arvanitis et al. [2020], Sarkaria et al. [2017]. Although the endothelial barrier is structurally compromised in some regions, drug delivery remains inefficient due to the heterogeneous permeability of the BBTB, poor perfusion caused by abnormal angiogenesis, and the presence of vessels that lack proper branching and fail to distribute drugs uniformly across the tumour Steeg [2021], Arvanitis et al. [2020].

Pericytes Of The BBTB: In glioblastoma, pericyte coverage along the vasculature is frequently reduced or structurally altered, contributing to the compromised integrity of the BBTB van Tellingen et al. [2015], Arvanitis et al. [2020]. This reduction is particularly evident in regions of tumour infiltration, where non-uniform pericyte distribution correlates with increased vascular permeability and diminished tight junction expression Arvanitis et al. [2020]. The loss of pericytic support destabilises endothelial cells and weakens the barrier's resistance to paracellular leakage Arvanitis et al. [2020], Steeg [2021].

Interactions between glioma cells and pericytes further exacerbate BBTB dysfunction. Colonisation of the abluminal surface by tumour cells induces oxidative stress and initiates autophagic signalling in pericytes, promoting immunosuppressive phenotypes that facilitate tumour progression Steeg [2021]. These stress responses compromise pericyte function and contribute to the breakdown of neurovascular unit integrity Steeg [2021].

Pericyte loss has also been observed in radiation necrosis following glioblastoma therapy, suggesting that therapeutic interventions may further impair BBTB stability van Tellingen et al. [2015]. Additionally, changes in basement membrane composition, particularly the loss of astrocytic laminin $\alpha 2$, disrupt pericyte anchorage and differentiation, weakening their ability to support endothelial barrier properties Steeg [2021].

Importantly, clinical data indicate that reduced pericyte coverage is associated with a poorer prognosis in glioblastoma patients undergoing chemotherapy, underscoring the translational relevance of pericyte integrity in BBTB function and therapeutic response Steeg [2021].

Astrocytes Of The BBTB: In glioblastoma, astrocytic regulation of the vascular interface is profoundly disrupted, contributing to the breakdown of the BBB Watkins et al. [2014], van Tellingen et al. [2015]. One of the

earliest and most spatially extensive changes is the displacement of astrocytic endfeet from the vascular surface by invading glioma cells Watkins et al. [2014], van Tellingen et al. [2015]. This physical uncoupling impairs astrocyte-mediated regulation of endothelial tight junctions and vascular tone, both of which are essential for maintaining barrier integrity Watkins et al. [2014].

The loss of astrocytic contact results in a focal reduction in tight junction proteins, such as claudin-5 and ZO-1, even in vessels distant from the tumour core Watkins et al. [2014]. These changes are sufficient to permit extravasation of macromolecules, including albumin and cadaverine, indicating that astrocyte displacement alone can compromise BBTB function Watkins et al. [2014]. In mouse models, even a single glioma cell in contact with a vessel was sufficient to induce local leakage of fluorescent tracers, demonstrating the barrier's sensitivity to astrocytic displacement Watkins et al. [2014].

In addition to functional uncoupling, glioblastoma induces molecular changes in astrocytes that further impair their barrier-supporting roles. Mislocalization and downregulation of aquaporin-4 (AQP4) from the astrocytic endfeet into non-polarised membrane domains have been observed in both glioblastoma and brain metastases, contributing to peritumoral oedema and exacerbating BBB dysfunction van Tellingen et al. [2015], Arvanitis et al. [2020]. In regions of glioblastoma that exhibit contrast enhancement on MRI—indicative of blood-brain barrier disruption—perivascular astrocytes appear disorganised and lose their typical association with the vasculature. In contrast, non-enhancing areas and low-grade gliomas retain a relatively preserved astrocytic distribution, consistent with an intact BBB Steeg [2021].

Reactive astrocytes at the tumour margin accumulate to form a dense glial structure that interacts bidirectionally with glioma cells Steeg [2021]. Rather than acting as a protective barrier, this astrocytic response contributes to tumour progression by promoting angiogenesis and invasion Steeg [2021]. Mechanistically, neuroinflammatory astrocytes upregulate sphingosine-1-phosphate receptor 3 (S1P3), leading to increased secretion of IL-6 and CCL2. These cytokines induce endothelial cells to downregulate tight and adherens junction proteins, thereby increasing paracellular permeability of the BBTB Steeg [2021].

Together, these structural and molecular changes reflect a progressive dismantling of astrocyte–vascular interactions in glioblastoma Watkins et al. [2014]. While this contributes to local barrier breakdown, it does not ensure sufficient drug penetration, particularly in infiltrative regions where the BBB remains relatively intact van Tellingen et al. [2015].

CD93 & MFSD2A: **CD93** is a transmembrane glycoprotein that is highly expressed in the vasculature of glioblastoma, with minimal expression in normal brain tissue and lower-grade gliomas Langenkamp et al. [2015]. Its expression correlates with tumour grade and poor survival in patients with high-grade astrocytic gliomas Langenkamp et al. [2015]. CD93-positive vessels are found in both the core and the invasive rim of glioblastoma, and their absence in mouse models leads to delayed tumour growth, increased vascular permeability, and reduced perfusion, indicating impaired vessel functionality Langenkamp et al. [2015].

Functionally, CD93 regulates endothelial cell–cell and cell–matrix adhesion, migration, and cytoskeletal organisation, all of which are essential for angiogenesis and the formation of stable tumour vasculature Barbera

et al. [2021], Lugano et al. [2023]. CD93 interacts directly with VE-cadherin and modulates junctional stability through Rho/ROCK-dependent signalling. Downregulation of CD93 results in phosphorylation and internalisation of VE-cadherin, displacement of claudin-5 from junctions, and formation of intercellular gaps, leading to increased vascular permeability Barbera et al. [2021]. These effects are reversible upon ROCK inhibition, confirming the pathway's involvement in CD93-mediated junctional regulation Barbera et al. [2021]. These findings suggest that CD93 might contribute to the formation of functional tumour vessels and may represent a therapeutic target for modulating glioblastoma vascular integrity.

MFSD2A is a lipid transporter selectively expressed in CNS endothelial cells, where it suppresses caveolae-mediated transcytosis and maintains BBB integrity Ocak et al. [2020]. In glioblastoma, MFSD2A expression is reduced in tumour-associated endothelial cells, with a clear distinction between the two GBM-EC subtypes. GBM-EC type 1, which displays high vascular permeability and elevated PLVAP levels, shows markedly decreased MFSD2A and claudin-5 expression, indicating a severely compromised barrier phenotype Xie et al. [2024]. In contrast, GBM-EC type 2 retains higher levels of MFSD2A and claudin-5, suggesting a more preserved BBB-like profile Xie et al. [2024].

Experimental overexpression of MFSD2A has been shown to restore tight junction integrity, increase claudin-5 and occludin levels, and suppress caveolin-1 expression, thereby reducing transcytosis and improving barrier function Ocak et al. [2020]. Conversely, downregulation of MFSD2A leads to increased endothelial leakage and worsened neurological outcomes Ocak et al. [2020]. These findings suggest that MFSD2A may be a key regulator of vascular integrity in glioblastoma and a potential therapeutic target for enhancing drug delivery across the blood–tumour barrier.

5 Hypothesis and Aim

Hypotheses

1. **Glioblastoma-induced disruption of the blood-brain barrier:**
   Glioblastoma disrupts the blood-brain barrier by downregulating the tight junction proteins claudin-5 and ZO-1, thereby increasing paracellular permeability and compromising barrier integrity.

2. **Correlation between CD93 and MFSD2A expression and barrier integrity:**
   The expression levels of CD93 and MFSD2A correlate with blood-brain tumour barrier integrity in glioblastoma. Specifically, elevated CD93 expression is associated with increased vascular permeability, while higher MFSD2A expression supports tight junction stability.

Research Aims

This study aims to elucidate the molecular mechanisms by which glioblastoma affects blood-brain barrier (BBB) integrity, with a particular focus on the roles of CD93 and MFSD2A. To address the proposed hypotheses, the following objectives will be pursued:

1. To isolate porcine brain capillary endothelial cells and establish in vitro BBB models that mimic key structural and functional features of the neurovascular unit.

2. To evaluate barrier integrity in these models using transendothelial electrical resistance (TEER) measurements.

3. To pharmacologically inhibit the expression of CD93 and MFSD2A and assess their impact on barrier function.

4. To quantify the gene expression levels of *claudin-5*, *ZO-1*, *CD93*, and *MFSD2A* using reverse transcription quantitative polymerase chain reaction.

5. To determine the protein expression of claudin-5 by quantitative Western blot analysis.

6 Materials and methods

6.1 Sample information

U87 is a human glioblastoma cell line originally established in 1966 at Uppsala University, Sweden, from a 44-year-old female patient diagnosed with malignant glioma. It has since become one of the most widely used in vitro models for glioblastoma research. However, discrepancies exist between versions distributed by different repositories. The European Collection of Authenticated Cell Cultures maintains that U87MG is of female origin. At the same time, the American Type Culture Collection version HTB-14 has been reported to carry a Y chromosome, suggesting male origin [Pokorná et al., 2021, Allen et al., 2016]. Moreover, prolonged passaging of U87MG has been shown to induce chromosomal aberrations and alter gene expression profiles, potentially diverging from the original tumour's phenotypic and molecular characteristics [Pokorná et al., 2021, Allen et al., 2016].

T10 is a more recently established human glioblastoma cell line, derived in 2019 from a patient at Rigshospitalet, Denmark. The cell line was made available for this study through a collaboration with Kræftens Bekæmpelse (the Danish Cancer Society). Due to its relatively low passage number, T10 is presumed to retain many of the original tumour's phenotypic and molecular characteristics, making it a valuable model for studying glioblastoma biology with minimal culture-induced alterations [Torsvik et al., 2014].

6.2 Primary Astrocyte cell culturing

Primary porcine astrocytes were thawed from cryopreserved stocks. Cells were maintained in Dulbecco's Modified Eagle Medium (DMEM, low glucose; Invitrogen, Cat. No. 21885025) supplemented with 10% fetal calf serum (FCS; Gibco, Cat. No. 10106-169) and 0.02% gentamicin sulfate (Lonza, Cat. No. 17-518Z). The complete medium was sterile-filtered and stored at 4°C.

Tissue culture-treated 12-well plates were pre-coated with poly-L-lysine (500 μg/mL) by incubating the coating solution at 37°C for approximately 2 hours. After incubation, the coating solution was removed, and the plates were allowed to dry under sterile conditions.

Thawed astrocytes were seeded into the coated wells at a density of 30.000 cells/cm^3. Cultures were maintained at 37°C in a humidified incubator with 5% CO_2. The medium was changed once or twice a week. For passaging, cells were detached using trypsin and reseeded following standard procedures.

6.3 T10 and U87 cell culturing

Before thawing the glioblastoma cell lines T10 and U87, the cultivation medium was prepared. The T10 and U87 medium consisted of 200 mL Neurobasal-A medium (Gibco|Thermo Fisher Scientific, Cat. No. 10888-022) with 2 mL penicillin/streptomycin solution (100X) (Gibco|Thermo Fisher Scientific, Cat. No. 15140-122), 1 mL N2 supplement (100X) (Gibco|Thermo Fisher Scientific, Cat. No. 17502-048), 2 mL B27 supplement without

vitamin A (50X) (Gibco|Thermo Fisher Scientific, Cat. No. 12587-010), 2 mL L-glutamine 200 mM, 0.05 mL basic fibroblast growth factor (bFGF; PeproTech, Cat. No. 100-18B, 0.1 mg/mL), and 0.25 mL epidermal growth factor (EGF; Sigma-Aldrich, Cat. No. E9644, 20 μg/mL). The medium was sterile-filtered and stored at 4°C for up to two weeks.

The cell lines T10 and U87 were thawed and transferred to two 15 mL tubes containing 10 mL phosphate-buffered saline (PBS) and centrifuged at 300 x g for 5 minutes at 21°C. The supernatant was discarded, and the cell pellet was resuspended in T10 and U87 medium and transferred to cell culture flasks. Cells were incubated at 37°C with 5% CO_2. Both T10 and U87 cell lines form spheroids, and to prevent necrosis from occurring within the spheroids, the medium was replaced 2-3 times a week, and the cells were passaged when they reached confluency.

6.4 In vitro Blood-Brain Barrier and Blood-Brain Tumour Barrier models

6.4.1 Isolation of primary porcine brain capillary endothelial cells

Twelve brain hemispheres from 6-month-old domestic pigs were obtained (Sæby Gårdslagteri I/S, Sæby), and the meninges were removed within hours after termination of the animals. 12 grams of gray matter tissue were harvested and transferred to a Petri dish containing 4 mL of DMEM/F12 medium (Gibco|Thermo Fisher Scientific, USA; Cat. No. 31331-028) on ice. The tissue was cut into 1 mm^3 pieces and transferred to a 50 mL tube and thoroughly mixed in a solution of DMEM/F12, supplemented with 1 mg/mL Collagenase type 2 (Gibco|Thermo Fisher Scientific, USA; Cat. No. 17101105) and 15 μg/mL Deoxyribonuclease I (DNase I) (Sigma-Aldrich, USA; Cat. No. D4513). The homogenate was incubated at 37°C in a shaker at 200 rpm for 1 hour and 15 minutes.

During the enzymatic digestion, a 33% Percoll gradient was prepared containing 57 mL PBS, 3 mL 10x PBS, 3 mL fetal calf serum (FCS), and 30 mL Percoll (Sigma-Aldrich, Cat. No. P1644). The solution was transferred into 50 mL Oak Ridge centrifuge tubes (NALGENE, Cat. No. 3118-0050) and weighed with a 1–2 μg difference between tubes and centrifuged at 30,000 x g for 1 hour at 4°C.

After incubation of the first enzymatic digestion, 10 mL of DMEM/F12 was added to the homogenate to prevent additional degradation and centrifuged at 1000 x g for 8 minutes at 4°C. The supernatant was removed and the cell pellet was resuspended in a 20 mL 20% bovine serum albumin (BSA) in DMEM solution (Europa Bioproducts, Cat. No. EQBAH62) and centrifuged at 1000 x g for 20 minutes at 4°C. After centrifugation, the supernatant containing the myelin layer with neurons and glial cells was discarded. The cell pellet was resuspended in 2 mL of DMEM/F12 medium and transferred to a new 50 mL tube.

For the last enzymatic digestion, a solution of DMEM/F12, supplemented with 1 mg/mL Collagenase-dispase (Roche, Switzerland; Cat. No. 1109113) and 6.67 μg/mL DNase I (Sigma-Aldrich, Cat. No. D4513) was added to the 50 mL tube, thoroughly mixed, and incubated at 37°C in a shaker at 200 rpm for 50 minutes. 10 mL of DMEM/F12 medium was added to the homogenate to prevent further degradation and centrifuged at 700 x g for 5 minutes at 4°C. The supernatant was discarded, 2 mL of DMEM/F12 was added and meticulously mixed with the cell pellet. 1 mL of cell suspension was carefully layered on top of the Percoll gradient in Oak Ridge tubes and centrifuged at 1000 x g for 10 minutes at 4°C.

During centrifugation, two 50 mL tubes with 25 mL of DMEM/F12 were prepared. After centrifugation, the Percoll gradient in the Oak Ridge tube appears pinkish in the top layer, followed by a cloudy white interface layer containing capillary fragments, and a red bottom layer comprising red blood cells and pericytes. The hazy white layer right on top of the red layer was carefully collected as seen in Figure 3A and transferred to the tubes containing the 25 mL DMEM/F12, followed by centrifugation at 1000 x g for 10 minutes at 4°C.

The supernatant was removed after centrifugation and the cell pellet containing the isolated microvessels was re-suspended in 27 mL PBCEC culture medium containing DMEM/F12, 10% Plasma Derived Bovine Serum (PDS) (First Link Ltd, UK), 10 μg/mL Insulin-Transferrin-Selenium (ITS) (Roche, Cat. No. 11074547001), 0.5 mg/mL Gentamicin (LONZA, Cat. No. 17-518Z), 0.0004 μg/mL puromycin (Sigma-Aldrich, Cat. No. P8833 or P7255), 0.015 μg/mL chloramphenicol (Kemikalierum/Svend), 0.1 ng/mL bFGF (Roche, Cat. No. 1363697), and transferred to 60 mm culture dishes (Hounisen, Cat. No. 83.1800) precoated with 50 μg/mL fibronectin (Sigma-Aldrich, Cat. No. F1141) and 150 μg/mL collagen-IV (Sigma-Aldrich, Cat. No. C5533) in Milli-Q water.

The culture dishes were then incubated for 2–3 days at 37°C with 5% CO_2. During the incubation, the endothelial cells migrate out of the vessel fragments as seen in Figure 3B. When the endothelial cells had reached a cell confluency of 70–80%, the cells were harvested and frozen at –70°C in freezing medium containing PBCEC medium with 30% FCS and 7.5% DMSO. After freezing for 3 days at -70°C the cells were transferred to a cryotank for long-term storage at -150°C.

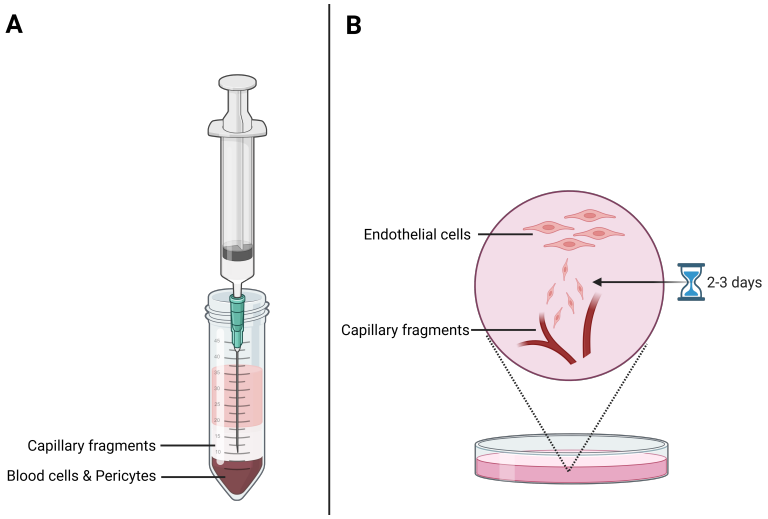

Figure 3: Isolation of primary porcine brain capillary endothelial cells (PBCECs). (**A**) Schematic representation of the capillary-rich white interface layer containing microvascular fragments collected from the Percoll density gradient after removal of the myelin-rich supernatant. (**B**) Schematic representation of endothelial cells migrating out from microvessel fragments after plating on fibronectin/collagen IV-coated culture dishes. Cells were maintained in PBCEC culture medium supplemented with growth factors and antibiotics until confluency 70–80%. Created in BioRender.com.

6.4.2 Establishing the Porcine Blood-Brain and Blood-Brain Tumour Barrier Models

The composition of the porcine barrier models was 12-well plates (Greiner CELLSTAR) with 1.12 cm^2 Transwell filter inserts (665610, Greiner Bio-One) with a pore diameter of 1μm seeded with approximately 100.000 PBCECs pr. cm^2 . Before seeding of the PBCEC's the filter inserts were coated with a coating solution containing sterile MiliQ, supplemented with 0.5 mg/mL collagen IV, 0.1 mg/mL fibronectin and incubated for 24 hours at 37°C with 5 % CO_2. The PBCECs were seeded into the filter inserts in 750 μL PBCEC medium along with 750 μL PBCEC medium in the well and incubated for 24 hours at 37°C with 5 % CO_2 followed by Trans-Endothelial Electrical Resistance (TEER) measurement. In this thesis, a total of four different barrier constructs were utilised, one with PBCECs in monoculture and three different PBCECs no contact co-cultures with either T10, U87 or astrocytes.

The induction of TJ formation was initiated when the PBCEC had formed a uniform layer with TEER values between 25-50 $\Omega \cdot cm^2$. The medium was removed and washed twice in 1x sterile PBS before replacing the medium in the filters with 750 μL PBCEC medium supplemented with 550 nM hydrocortisone (H4001, Sigma Aldrich), 250 μM pCPT-cAMP (C3912, Sigma Aldrich) and 17.5 μM RO-20-1724 (B8279, Sigma Aldrich). In the bottom well, the medium was replaced with 1.5 mL PBCEC medium supplemented with 550 nM hydrocortisone for monocultures. For co-cultures, a mix of 50/50 PBCEC medium supplemented with 550 and either Neurobasal-A medium for wells with GBM cells or astrocyte medium for wells with astrocytes. The seeding density for both GBMs and astrocytes was 30.000 cells pr cm^2.

6.5 Trans-Endothelial Electrical Resistance

TEER was measured daily to assess the integrity of the barrier models using a Millicell ERS-2 Epithelial Volt-Ohm Meter (Millipore, MERS00002) equipped with a Millicell ERS-STX01 electrode (Millipore, MERSSTX01). Before measuring the experimental inserts, a blank well containing only cell culture medium and an insert without cells was measured three times to establish a baseline resistance value for calibration.

Each experimental insert was measured three times by carefully placing the electrode into the insert and the surrounding well medium. The average of the three readings was calculated and multiplied by the surface area of the insert (1.12 cm^2) to obtain the TEER value in $\Omega \cdot cm^2$. To correct for background resistance, the average value from the blank insert measurements was subtracted from each sample's calculated TEER.

6.6 Inhibition of MFSD2A & CD93

To investigate the role of *MFSD2A* and *CD93* in endothelial barrier integrity, primary endothelial cells were cultured on 12 mm transwell inserts with 1 μm pore polycarbonate membranes for 12 days. However, from now on, day 3 will be considered day 1, as this is when the first TEER measurements were conducted (Figure 4). *MFSD2A* was inhibited at day (8) using tunicamycin (TM), diluted in culture medium to a final concentration of 1 µg/mL [Xu et al., 2024], and applied to the PBCECs in the upper chamber for 24 hours at 37°C in a humidified incubator with 5% CO_2. This approach is based on a study by Xu et al. [Xu et al., 2024] demonstrating that

TM-induced *MFSD2A* inhibition disrupts endothelial barrier function by modulating tight junction integrity [Xu et al., 2024].

To inhibit *CD93* signalling, metoclopramide was applied at a final concentration of 1 µM [Riether et al., 2021] in culture medium to the PBCECs in the upper chamber at day 11 and incubated for 24 hours at 37°C in a humidified incubator with 5% CO_2. This approach is based on a study by Riether et al. [Riether et al., 2021].

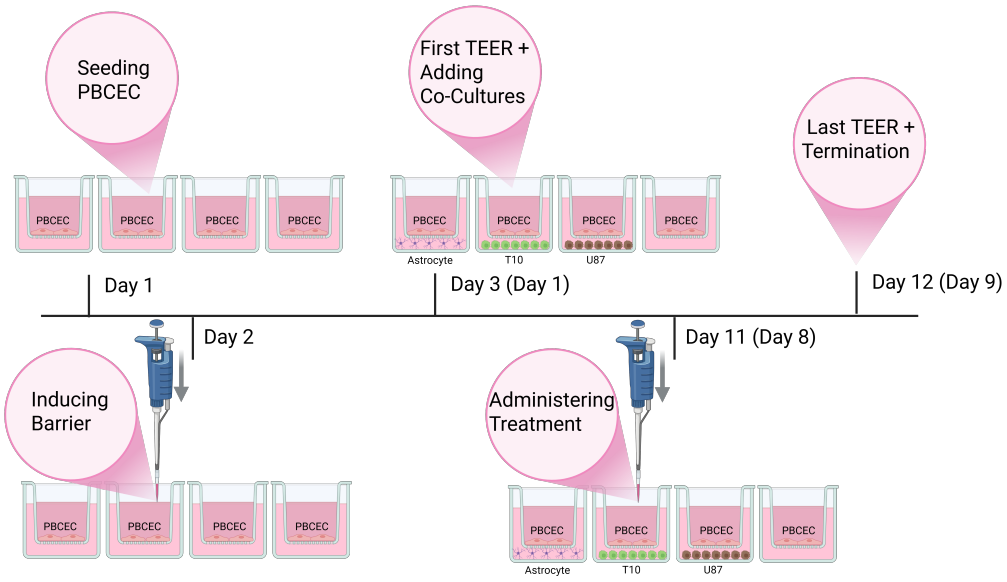

Figure 4: Experimental timeline for the primary porcine brain capillary endothelial cell (PBCEC) co-culture study. On Day 1, PBCECs were seeded onto transwell inserts. On Day 2, barrier properties were induced by adding barrier-promoting supplements to the culture medium. On Day 3, the first transendothelial electrical resistance (TEER) measurements were taken, and co-cultures with astrocytes, T10 glioblastoma cells, or U87 glioblastoma cells were established. Between Days 3 (1) and 11 (8), co-cultures were maintained under standard conditions. On Day 11, pharmacological treatments (Tunicamycin or Metoclopramide) were administered. On Day 12 (9), the final TEER measurements were recorded, followed by termination of the experiment and sample collection for downstream analyses. Created in BioRender.com.

6.7 Gene Expression Analysis Of Barrier Models

6.7.1 RNA Extraction & Purification

Total RNA was extracted from adherent cultured cells using the GeneJET RNA Purification Kit (Thermo Scientific, K0731), following the manufacturer's protocol. Briefly, cells were cultured for 9 days, after which the growth medium was removed and the cells were rinsed once with phosphate-buffered saline (PBS) to eliminate residual

medium. Cells were then detached by scraping in PBS and pelleted by centrifugation at 250 x g for 5 minutes. The cell pellet was resuspended in 400 μL of Lysis Buffer supplemented with 2% 14.3 M β-mercaptoethanol to inactivate RNases. Following homogenization, 240 μL of 96–100 % ethanol was added to the lysate and mixed thoroughly. The mixture was then transferred to a GeneJET RNA Purification Column and centrifuged at $\geq$12.000 x g for 1 minute. After discarding the flow-through, the column was washed with 700 μL of Wash Buffer 1 and centrifuged at $\geq$12.000 g for 1 minute. This was followed by a wash with 600 μL of Wash Buffer 2, centrifuged at $\geq$12.000 x g for 1 minute, and a final wash with 250 μL of Wash Buffer 2, centrifuged at $\geq$12.000 x g for 2 minutes to ensure complete removal of residual buffer. RNA was eluted by adding 25 μL of nuclease-free water directly to the centre of the column membrane and centrifuging at $\geq$12.000 x g for 1 minute. This step was repeated to a total volume of 50 μL. The concentration and purity of the eluted RNA were assessed using a NanoDrop spectrophotometer, and samples were stored at -70°C

6.7.2 cDNA Synthesis

To remove residual genomic DNA, 1 μg of total RNA was treated with 1 U of RNase-free DNase I (Thermo Scientific, EN0521) in a 10 μL reaction volume containing 1 μL of 10X DNase I Reaction Buffer with $MgCl_3$. The reaction was incubated at 37°C for 30 minutes, followed by inactivation with 1 μL of 50 mM EDTA and heating at 65°C for 10 minutes. First-strand cDNA synthesis was performed using the Maxima H Minus First Strand cDNA Synthesis Kit (Thermo Scientific, K1651). For each reaction, 1 μg of DNase-treated RNA was combined with 0.25 μL each of oligo(dT) and random hexamer primers (25 pmol), 1 μL of 10 mM dNTP mix, and nuclease-free water to a final volume of 15 μL. After primer annealing, 4 μL of 5X RT buffer and 1 μL of Maxima H Minus Enzyme Mix were added. The reverse transcription was carried out at 25°C for 10 minutes, followed by 50°C for 15 minutes, and terminated by heating at 85°C for 5 minutes. The resulting cDNA was stored at -20°C until downstream use in qPCR.

6.7.3 RT-qPCR

Primers used for RT-qPCR analysis were designed using Primer-BLAST from the National Centre for Biotechnology Information database and synthesised by Tag Copenhagen A/S. Primer sequences targeting human genes (used for T10 and U87 cell lines) are listed in Table 2, while those targeting porcine genes (used for BBB and BBTB models) are shown in Table 3. *GAPDH* and *HPRT1* were used as reference genes for normalisation of gene expression.

Quantitative real-time PCR (RT-qPCR) was performed using the Maxima SYBR Green qPCR Master Mix (2X) without ROX Solution (Thermo Scientific, K0252). Each 10 μL reaction contained 5 μL of 2X Master Mix, 0.3 μM of each forward and reverse primer, 5 μL of template containing 2 ng cDNA. ROX reference dye was not included, as the Bio-Rad CFX96 real-time PCR system used in this thesis does not necessitate ROX normalisation. Thermal cycling was performed under the following conditions: initial denaturation at 95°C for 10 minutes, followed by 40 cycles of 95°C for 15 seconds and 60°C for 60 seconds. Fluorescence data were collected

during the annealing/extension step. A melting curve analysis was performed at the end of each run to confirm the specificity of amplification. No-template controls (NTC) and reverse transcriptase-minus (RT-) controls were included to identify contamination and carryover of genomic DNA. Primer efficiencies were calculated using LinRegPCR software, which analyses raw fluorescence data to determine individual reaction efficiencies based on the linear regression of the exponential phase of amplification.

Table 1: Primer sequences used for RT-qPCR analysis of *Sus scrofa* Astrocyte and brain capillary endothelial cells. The table includes forward and reverse primer sequences for reference genes (*GAPDH* and *HPRT1*) and genes of interest (*Claudin-5*, *ZO-1*, *CD93* and *MFSD2A*).

Target	**Forward Sequence:**	**Reverse Sequence:**
GAPDH	CAGACAGCCGTGTGTTCCGT	TGCGGCCAAATCCGTTCACT
HPRT1	AAGCTGAAGCATTCTGGCTTTCGTC	CACACAGAGGGCTACAATGTGATGGC
Claudin-5	GTTGTGCTCCACCAACTGCAAATC	AACATGGCACCACACCATACATTC
ZO-1	AAGCCTCCAGAGGCAGACTATAA	AATCAGGGAAGCCATCACATGGG
CD93	ATGGGCCGGTTCTGGATTGG	GGCGTATCCTCCACGCCATC
MFSD2A	GTGAACGTCCGGTCCAGGTG	CGGAGAAAGGATCCACCTGAGCTA

Table 2: Primer sequences used for RT-qPCR analysis of *Homo sapiens* T10 and U87 cells. The table includes forward and reverse primer sequences for reference genes (*GAPDH* and *HPRT1*) and genes of interest (*CD93* and *MFSD2A*).

Target	**Forward Sequence:**	**Reverse Sequence:**
GAPDH	AAGACGGGCGGAGAGAAACC	CCCAATACGACCAAATCCGTTGAC
HPRT1	GCCCTGGCGTCGTGATTAGT	TGGCCCTCCCATCTCTCCTCATCA
CD93	CAAGCGGAGAGCGAAGAGGG	TGTCCCAGGTGTCGGACTGT
MFSD2A	CTACCAGGTGACGGGCTGTG	CAACTTCCTCATCCTTCTGAGCCA

6.8 Protein Expression Analysis of Barrier Models

6.8.1 Protein Extraction & Purification

PBCECs from the barrier were lysed using RIPA buffer (Thermo Scientific, 89900) supplemented with protease and phosphatase inhibitors (Sigma, 5892791001; Thermo Scientific, A32961), 10 mM sodium fluoride (NaF), and 1 U/μL Benzonase (Sigma, E1014-5KU). Cells were washed with PBS, and lysis buffer (approximately 70 μL per well for a 24-well plate) was added directly to the wells. The plate was incubated on ice for at least 20 minutes to ensure complete lysis. Lysates were then transferred to Eppendorf tubes and either stored at -20°C or used immediately for protein quantification.

Total protein concentration was determined using the Pierce BCA Protein Assay Kit (Thermo Scientific, 23225) according to the manufacturer's protocol. Briefly, 25 μL of each sample or BSA standard was mixed with 200 μL of working reagent (prepared by mixing Reagent A and Reagent B in a 50:1 ratio) in a 96-well plate. The plate was incubated at 37°C for 30 minutes, cooled to room temperature, and absorbance was measured at

562 nm using a microplate reader. Protein concentrations were calculated from a standard curve generated using serial dilutions of BSA.

6.8.2 SDS-Page

Protein samples were prepared by mixing with 4× Laemmli sample buffer containing β-mercaptoethanol and heating at 95°C for 4 minutes. Equal amounts of protein (typically 10–30 µg) were loaded onto 10% SDS-polyacrylamide gels prepared using the Laemmli buffer system. Electrophoresis was performed using the Bio-Rad Mini-PROTEAN Tetra Cell system at a constant voltage of 180 V for approximately 35-45 minutes in 1× Tris-Glycine-SDS running buffer.

Protein separation was performed using 8-16 % Mini-PROTEAN TGX Precast Protein Gels (Bio-Rad, 4561103), 10-well format with a 30 μL capacity per well. Before loading, protein samples were mixed with 4x Laemmli sample buffer containing β-mercaptoethanol and denatured by heating at 95°C for 4 minutes. Approximately 7.5 µg of total protein was loaded into each well. For molecular weight reference, 5 μL of LI-COR Chameleon Duo Pre-Stained Protein Ladder (928-60000) was included. Electrophoresis was performed using the Bio-Rad Mini-PROTEAN Tetra Cell system at a constant voltage of 180 V for approximately 45 minutes in 1× Tris-Glycine-SDS running buffer.

6.8.3 Quantitative Western Blot

Following SDS-PAGE, proteins were transferred to nitrocellulose membranes using a wet transfer method. The transfer buffer consisted of 1× Tris-Glycine supplemented with 20% methanol. Nitrocellulose membranes were pre-soaked in transfer buffer before assembly.

The blotting sandwich was assembled in the following order: two pre-wetted sponges, Whatman paper, the SDS gel (pre-equilibrated in transfer buffer for 2-3 minutes), the nitrocellulose membrane, and two additional layers of Whatman paper. Air bubbles were carefully removed by gently rolling from the centre outward. The sandwich was enclosed in a blotting cassette with the black side facing the cathode and inserted into the blotting apparatus, which was filled to the indicated maximum volume with cold transfer buffer. Blotting was performed at 100 V for 2 hours at 4°C with gentle stirring.

After transfer, membranes were dried overnight at room temperature on clean filter paper. The next day, membranes were rehydrated in TBS for 5 minutes at room temperature with gentle shaking, followed by a rinse in MiliQ water. Total protein staining was performed using Revert 700 Total Protein Stain (LI-COR). Membranes were incubated in 5 mL of stain solution for 5 minutes at room temperature with gentle shaking. The stain was then removed, and membranes were washed twice for 30 seconds each with 5 mL of Revert 700 Wash Solution (P/N 926-11012), followed by a brief rinse in MiliQ water.

Membranes were immediately imaged using the LI-COR Odyssey FC imaging system in the 700 nm channel. A linear range analysis was performed to ensure that the Claudin-5 antibody signal fell within the quantifiable dynamic range. After imaging, membranes were blocked in blocking buffer (20 mM Tris-base, 150 mM NaCl, 3%

gelatin, pH 7.5) for 30 minutes at 37°C with gentle agitation.

Following blocking, membranes were incubated overnight at 4°C with primary antibody (Claudin-5) diluted 1:1000 in antibody buffer (20 mM Tris-base, 150 mM NaCl, 0.2% gelatin, 0.05% Tween-20, pH 7.5). The next day, membranes were washed four times for 5 minutes each in TBS-T (1× TBS with 0.05% Tween-20) on a platform shaker at room temperature.

Secondary antibody incubation was performed using IRDye 800CW goat anti-rabbit antibody diluted 1:20.000 in antibody buffer. Membranes were incubated for 1 hour at room temperature with gentle shaking, followed by another four washes in TBS-T. A final rinse in 1× TBS was performed to remove residual Tween-20.

Final imaging was performed on the LI-COR Odyssey FC system. Quantification of protein bands was performed using LI-COR Empirica Studio software, with normalisation to the total protein signal obtained from Revert 700 staining.

6.9 Statistical Analysis

All statistical analyses were performed using GraphPad Prism version 10.5.0 (GraphPad Software, USA). Data are presented as mean ± standard error of the mean (SEM), unless otherwise indicated. Prior to hypothesis testing, data were evaluated for normality using the Shapiro-Wilk test. For comparisons involving multiple groups and time points, a two-way analysis of variance (ANOVA) was employed, followed by Tukey's multiple comparisons test. For endpoint comparisons, such as gene and protein expression, one-way ANOVA with Tukey's post hoc test was utilised. Statistical significance was defined as $p < 0.05$, with significance levels indicated as follows: $^{*}p < 0.05$, $^{**}p < 0.01$, $^{***}p < 0.001$, and $^{****}p < 0.0001$.

7 Results

7.1 TEER of of BBB and BBTB Models

To investigate how glioma-associated cells affect PBCEC barrier properties, TEER was measured in BBB and BBTB models over a 9-day period (Figure 5). The models included PBCEC monoculture, PBCEC co-cultured with astrocytes, and co-cultures with glioma cells (T10 or U87). These untreated conditions also serve as a reference for evaluating the effects of subsequent pharmacological treatments. Each condition was tested in two independent experimental runs ($n = 6$ per run), resulting in a total of $n = 12$ per group.

Days 1–2 (Start): At the beginning of the experiment, TEER values were relatively low across all conditions. On Day 1, PBCEC & T10 showed no difference from PBCEC ($-1.1\ \Omega \cdot \text{cm}^2$, $p > 0.9999$), while PBCEC & U87 had a non-significant increase ($+22.2\ \Omega \cdot \text{cm}^2$, $p = 0.8686$). PBCEC & Astrocyte also showed a non-significant reduction compared to PBCEC ($-22.5\ \Omega \cdot \text{cm}^2$, $p = 0.8468$).

By Day 2, PBCEC & T10 showed a significant TEER increase compared to PBCEC ($+147.1\ \Omega \cdot \text{cm}^2$, $p = 0.0006$), whereas PBCEC & U87 had a non-significant increase ($+75.1\ \Omega \cdot \text{cm}^2$, $p = 0.1596$). PBCEC & Astrocyte remained statistically similar to PBCEC ($-36.2\ \Omega \cdot \text{cm}^2$, $p = 0.3510$). PBCEC & T10 was significantly higher than PBCEC & Astrocyte ($+183.2\ \Omega \cdot \text{cm}^2$, $p < 0.0001$), and PBCEC & U87 was also elevated compared to PBCEC & Astrocyte ($+111.3\ \Omega \cdot \text{cm}^2$, $p = 0.0138$).

Days 4–5 (Mid): In the mid-phase, TEER values continued to rise in the glioma co-cultures. On Day 4, PBCEC & T10 was significantly higher than PBCEC ($+253.3\ \Omega \cdot \text{cm}^2$, $p < 0.0001$), while PBCEC & U87 showed a non-significant increase ($+62.8\ \Omega \cdot \text{cm}^2$, $p = 0.1375$). PBCEC & Astrocyte remained statistically similar to PBCEC ($-46.6\ \Omega \cdot \text{cm}^2$, $p = 0.1108$). PBCEC & T10 was significantly higher than PBCEC & U87 ($+190.4\ \Omega \cdot \text{cm}^2$, $p = 0.0005$) and PBCEC & Astrocyte ($+299.8\ \Omega \cdot \text{cm}^2$, $p < 0.0001$).

On Day 5, PBCEC & T10 remained significantly higher than PBCEC ($+274.9\ \Omega \cdot \text{cm}^2$, $p < 0.0001$), while PBCEC & U87 showed a significant increase ($+95.2\ \Omega \cdot \text{cm}^2$, $p = 0.0059$). PBCEC & Astrocyte remained statistically similar to PBCEC ($-37.6\ \Omega \cdot \text{cm}^2$, $p = 0.2656$). PBCEC & T10 was also significantly higher than PBCEC & U87 ($+179.7\ \Omega \cdot \text{cm}^2$, $p = 0.0007$) and PBCEC & Astrocyte ($+312.5\ \Omega \cdot \text{cm}^2$, $p < 0.0001$).

Days 8–9 (End): At the end of the experiment, PBCEC & T10 maintained the highest TEER values. On Day 8, it was significantly higher than PBCEC ($+402.3\ \Omega \cdot \text{cm}^2$, $p < 0.0001$), while PBCEC & U87 also showed a significant increase ($+203.1\ \Omega \cdot \text{cm}^2$, $p < 0.0001$). PBCEC & Astrocyte showed a modest but significant increase ($+62.1\ \Omega \cdot \text{cm}^2$, $p = 0.0086$). PBCEC & T10 was significantly higher than PBCEC & U87 ($+199.2\ \Omega \cdot \text{cm}^2$, $p = 0.0018$) and PBCEC & Astrocyte ($+340.2\ \Omega \cdot \text{cm}^2$, $p < 0.0001$).

On Day 9, the PBCEC & T10 co-culture exhibited the highest TEER increase relative to PBCEC monoculture ($+450.5\ \Omega \cdot \text{cm}^2$, $p < 0.0001$), while PBCEC & Astrocyte also showed a significant increase ($+78.9\ \Omega \cdot \text{cm}^2$, $p = 0.0023$). PBCEC & U87 also displayed a significant increase relative to PBCEC monoculture ($+212.3\ \Omega \cdot \text{cm}^2$,

$p = 0.0003$). The PBCEC & T10 remained significantly higher than PBCEC & U87 ($+238.2\ \Omega \cdot \text{cm}^2$, $p = 0.0047$) and PBCEC & Astrocyte ($+371.6\ \Omega \cdot \text{cm}^2$, $p < 0.0001$). A significant difference was observed between PBCEC & U87 and PBCEC & Astrocyte ($-133.3\ \Omega \cdot \text{cm}^2$, $p = 0.016$).

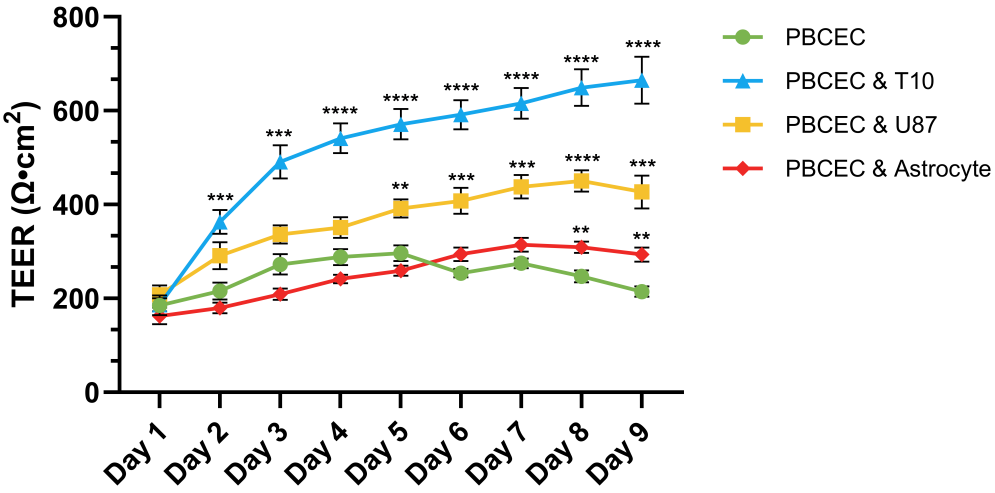

Figure 5: TEER measurements in BBB and BBTB in vitro models over 9 days. PBCEC and PBCEC & Astrocyte represent the BBB model, while PBCEC & T10 and PBCEC & U87 represent BBTB models. Each point shows the mean TEER value from two pooled experimental runs ($n = 12$ per group). Asterisks above time points indicate statistically significant differences between groups. Data are presented as mean ± SEM. Statistical analysis was performed using 2-way ANOVA followed by Tukey's multiple comparisons test. Asterisks indicate significance levels: * $p < 0.05$, ** $p < 0.01$, *** $p < 0.001$, **** $p < 0.0001$.

7.1.1 TEER in the Tunicamycin-treated Group

To assess the impact of MFSD2A inhibition on barrier integrity, Tunicamycin was used to inhibit MFSD2A by blocking N-linked glycosylation, thereby disrupting its lipid transport and barrier-stabilising functions. This inhibition is expected to increase caveolae-mediated transcytosis and reduce tight junction protein expression, leading to compromised barrier integrity and reduced TEER. As with the previous experiment, this experiment used a similar setup of BBB and BBTB models but were treated with Tunicamycin on Day 8 (Figure 6). TEER was measured in PBCEC monocultures and glioma co-cultures (T10 or U87), with data pooled from two independent runs ($n = 12$ per group).

Days 1–2 (Start): On Day 1, PBCEC & T10 Tunicamycin showed a modest but significant increase in TEER compared to PBCEC Tunicamycin ($+83.2\ \Omega \cdot \text{cm}^2$, $p = 0.0164$), while PBCEC & U87 Tunicamycin did not differ significantly ($+36.0\ \Omega \cdot \text{cm}^2$, $p = 0.4803$). The TEER values between PBCEC & T10 Tunicamycin and PBCEC & U87 Tunicamycin were statistically similar ($+47.2\ \Omega \cdot \text{cm}^2$, $p = 0.2700$).
By Day 2, the divergence between groups became more apparent. PBCEC & T10 Tunicamycin displayed a

pronounced and significant rise over PBCEC Tunicamycin (+252.8 $\Omega \cdot \text{cm}^2$, $p < 0.0001$), whereas PBCEC & U87 Tunicamycin remained non-significant (+37.5 $\Omega \cdot \text{cm}^2$, $p = 0.5839$). TEER in PBCEC & T10 Tunicamycin exceeded that of PBCEC & U87 Tunicamycin by a substantial margin (+215.3 $\Omega \cdot \text{cm}^2$, $p < 0.0001$).

Day 7 (Mid): By Day 7, TEER values peaked in the glioma co-cultures. PBCEC & T10 Tunicamycin exhibited a marked increase compared to PBCEC Tunicamycin (+587.3 $\Omega \cdot \text{cm}^2$, $p < 0.0001$), and PBCEC & U87 Tunicamycin also showed a significant elevation (+166.6 $\Omega \cdot \text{cm}^2$, $p = 0.0007$). The difference between the two glioma co-cultures was highly significant, with PBCEC & T10 Tunicamycin surpassing PBCEC & U87 Tunicamycin by +420.6 $\Omega \cdot \text{cm}^2$ ($p < 0.0001$).

Days 8–9 (End): At the end of the experiment, PBCEC & T10 Tunicamycin retained the highest TEER values. On Day 8, it was significantly greater than PBCEC Tunicamycin (+579.0 $\Omega \cdot \text{cm}^2$, $p < 0.0001$), and PBCEC & U87 Tunicamycin was also elevated (+200.1 $\Omega \cdot \text{cm}^2$, $p = 0.0002$). PBCEC & T10 Tunicamycin remained well above PBCEC & U87 Tunicamycin (+378.9 $\Omega \cdot \text{cm}^2$, $p < 0.0001$).
On Day 9, PBCEC & T10 Tunicamycin continued to display significantly higher TEER than PBCEC Tunicamycin (+520.2 $\Omega \cdot \text{cm}^2$, $p < 0.0001$), with PBCEC & U87 Tunicamycin also significantly elevated (+177.2 $\Omega \cdot \text{cm}^2$, $p = 0.0008$). The differences between PBCEC & T10 Tunicamycin and PBCEC & U87 Tunicamycin remained significant (+343.1 $\Omega \cdot \text{cm}^2$, $p < 0.0001$).

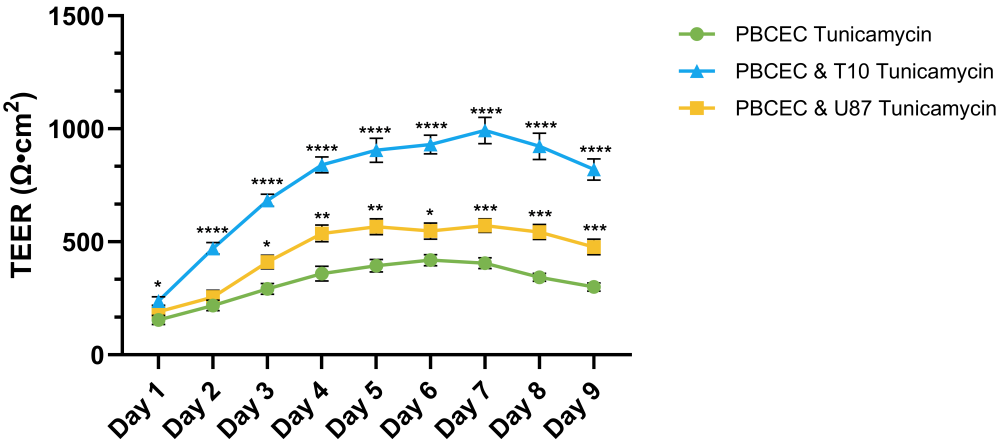

Figure 6: TEER measurements in BBB and BBTB in vitro models treated with Tunicamycin on Day 8. PBCEC and glioma co-cultures (PBCEC & T10, PBCEC & U87) were monitored over 9 days. Each point shows the mean TEER value from two pooled experimental runs ($n = 12$ per group). Asterisks above time points indicate statistically significant differences between groups. Data are presented as mean ± SEM. Statistical analysis was performed using 2-way ANOVA followed by Tukey's multiple comparisons test. Asterisks indicate significance levels: * $p < 0.05$, ** $p < 0.01$, *** $p < 0.001$, **** $p < 0.0001$.

7.1.2 TEER in the Metoclopramide-treated Group

To assess the impact of CD93 inhibition on barrier functionality, Metoclopramide was employed to obstruct CD93 signalling by preventing the nuclear translocation of its intracellular domain, which is recognised for its role in maintaining endothelial junction stability. This inhibition is projected to elevate VE-cadherin phosphorylation and turnover, consequently weakening adherens junctions and indirectly causing disorganisation of tight junctions. Consequently, barrier integrity is expected to diminish, as indicated by a reduction in TEER. TEER was measured in PBCEC monocultures and glioma co-cultures (T10 or U87) subsequent to Metoclopramide administration on Day 8 (Figure 7). As with previous conditions, data were pooled from two experimental runs ($n = 12$ per group).

Days 1–2 (Start): On Day 1, PBCEC & T10 showed a modest but significant increase in TEER compared to PBCEC (+88.7 $\Omega \cdot \text{cm}^2$, $p = 0.0158$), while PBCEC & U87 was not significantly different (+47.3 $\Omega \cdot \text{cm}^2$, $p = 0.3364$). The difference between PBCEC & T10 and PBCEC & U87 was not significant (+41.4 $\Omega \cdot \text{cm}^2$, $p = 0.4482$). By Day 2, the differences became more pronounced. PBCEC & T10 showed a significant increase over PBCEC (+221.5 $\Omega \cdot \text{cm}^2$, $p < 0.0001$), while PBCEC & U87 remained non-significant (+75.8 $\Omega \cdot \text{cm}^2$, $p = 0.1865$). PBCEC & T10 was also significantly higher than PBCEC & U87 (+145.7 $\Omega \cdot \text{cm}^2$, $p = 0.0065$).

Day 7 (Mid): By Day 7, TEER values peaked in the glioma co-cultures. PBCEC & T10 showed a substantial increase compared to PBCEC (+512.6 $\Omega \cdot \text{cm}^2$, $p < 0.0001$), and PBCEC & U87 also showed a significant increase (+210.4 $\Omega \cdot \text{cm}^2$, $p = 0.0025$). PBCEC & T10 was significantly higher than PBCEC & U87 (+302.2 $\Omega \cdot \text{cm}^2$, $p < 0.0001$).

Days 8–9 (End): At the end of the experiment, PBCEC & T10 maintained the highest TEER values. On Day 8, it was significantly higher than PBCEC (+498.3 $\Omega \cdot \text{cm}^2$, $p < 0.0001$), and PBCEC & U87 also showed a significant increase (+162.5 $\Omega \cdot \text{cm}^2$, $p = 0.0094$). PBCEC & T10 was significantly higher than PBCEC & U87 (+335.8 $\Omega \cdot \text{cm}^2$, $p < 0.0001$).
On Day 9, PBCEC & T10 remained significantly elevated over PBCEC (+455.9 $\Omega \cdot \text{cm}^2$, $p < 0.0001$), while PBCEC & U87 were not significantly different from PBCEC (+102.4 $\Omega \cdot \text{cm}^2$, $p = 0.1786$). PBCEC & T10 was still significantly higher than PBCEC & U87 (+353.5 $\Omega \cdot \text{cm}^2$, $p < 0.0001$).

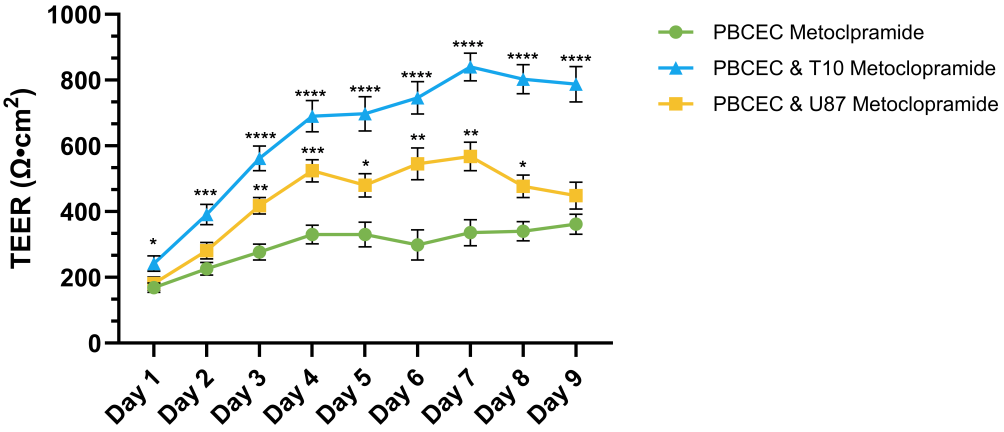

Figure 7: TEER measurements in BBB and BBTB in vitro models treated with Metoclopramide on Day 8. PBCEC and glioma co-cultures (PBCEC & T10, PBCEC & U87) were monitored over 9 days. Each point shows the mean TEER value from two pooled experimental runs ($n = 12$ per group). Asterisks above time points indicate statistically significant differences between groups. Data are presented as mean ± SEM. Statistical analysis was performed using 2-way ANOVA followed by Tukey's multiple comparisons test. Asterisks indicate significance levels: * $p < 0.05$, ** $p < 0.01$, *** $p < 0.001$, **** $p < 0.0001$.

7.2 Gene Expression of BBB and BBTB Models

To investigate differences in gene expression between BBB and BBTB in vitro models, four genes associated with endothelial integrity and function were analysed: *Claudin-5*, *ZO-1*, *MFSD2A*, and *CD93*. The BBB model consisted of PBCEC in monoculture or co-culture with astrocytes. The BBTB models included PBCEC co-cultured with either T10 or U87 glioblastoma-associated cells Figure 8).

Due to limited RNA yield from individual filter inserts, three inserts were pooled to generate a single biological replicate. Each condition was represented by two biological replicates ($n = 2$), resulting in six inserts per condition.

For *Claudin-5*, significant differences in expression were observed between several conditions. Expression was significantly increased in PBCEC co-cultured with T10 compared to PBCEC monoculture, with a mean difference of -2.953 (adjusted $p = 0.0006$). Similarly, PBCEC co-cultured with U87 showed a significant increase compared to PBCEC, with a mean difference of -2.796 (adjusted $p = 0.0011$). No significant difference was found between PBCEC and PBCEC co-cultured with astrocytes (adjusted $p = 0.8027$). However, both PBCEC & T10 and PBCEC & U87 exhibited significantly higher *Claudin-5* expression than PBCEC & Astrocyte, with mean differences of 3.484 (adjusted $p = 0.0001$) and 3.327 (adjusted $p = 0.0002$), respectively. No significant difference was observed between PBCEC & T10 and PBCEC & U87 (adjusted $p = 0.9930$).

For *CD93*, expression was significantly increased in PBCEC & U87 compared to PBCEC, with a mean difference of -1.694 (adjusted $p = 0.0476$). Additionally, PBCEC & T10 and PBCEC & U87 both showed significantly higher expression than PBCEC & Astrocyte, with mean differences of 1.797 (adjusted $p = 0.0339$)

and 2.194 (adjusted $p = 0.0087$), respectively. No significant differences were observed between PBCEC and PBCEC & T10 (adjusted $p = 0.1628$), or between PBCEC & T10 and PBCEC & U87 (adjusted $p = 0.9044$).

In contrast, *ZO-1* and *MFSD2A* did not show any statistically significant differences in expression across the tested conditions (all adjusted $p > 0.05$).

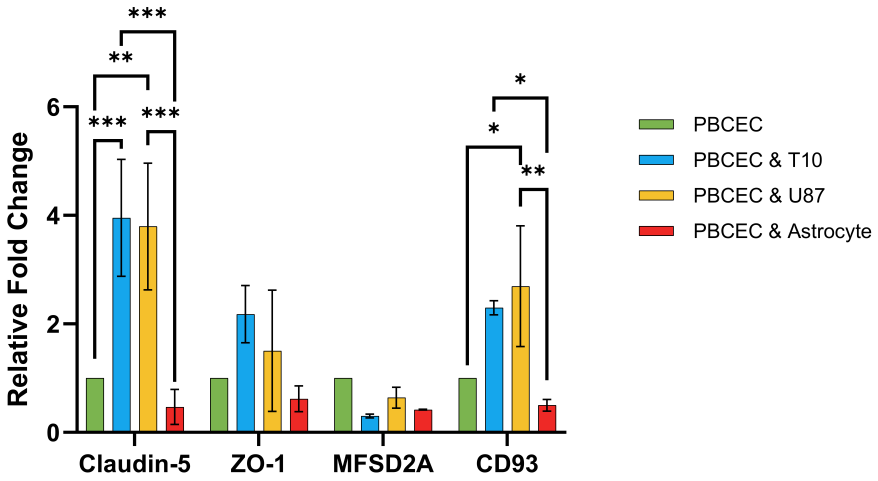

Figure 8: Relative mRNA expression of *Claudin-5*, *ZO-1*, *MFSD2A*, and *CD93* in BBB and BBTB in vitro models. PBCEC and PBCEC + Astrocyte represent the BBB model, while PBCEC & T10 and PBCEC & U87 represent BBTB models. Each bar shows the mean relative expression (normalised to PBCEC) from two biological replicates ($n = 2$), where each replicate was generated by pooling RNA from three filter inserts to ensure sufficient material for RT-qPCR. *Claudin-5* expression was significantly upregulated in PBCEC & T10 and PBCEC & U87 compared to PBCEC alone (***, $p < 0.001$ and **, $p < 0.01$, respectively). *CD93* was significantly upregulated in PBCEC & U87 compared to PBCEC (*, $p < 0.05$). No significant differences were observed for *ZO-1* or *MFSD2A*. Data are presented as mean ± SEM. Statistical analysis was performed using 2-way ANOVA followed by Tukey's multiple comparisons test. Asterisks indicate significance levels: * $p < 0.05$, ** $p < 0.01$, *** $p < 0.001$.

7.2.1 Expression after Tunicamycin treatment

To explore whether inhibition of *MFSD2A* affects tight junction gene expression, BBB and BBTB models were treated with Tunicamycin. The analysis focused on the mRNA expression of *Claudin-5*, *ZO-1*, and *MFSD2A* (Figure 9). Each condition was represented by two biological replicates, with RNA pooled from three filter inserts per replicate.

Claudin-5 expression was significantly upregulated in the PBCEC & T10 Tunicamycin group compared to PBCEC monoculture (mean difference = −2.63, adjusted $p = 0.0384$). Additionally, PBCEC treated with Tunicamycin showed significantly lower Claudin-5 expression than PBCEC & T10 (mean difference = 3.50, adjusted $p = 0.0039$) and PBCEC & U87 (mean difference = 3.35, adjusted $p = 0.0059$). A significant difference was also observed between PBCEC Tunicamycin and PBCEC & T10 Tunicamycin (mean difference = −3.18,

adjusted $p = 0.0092$).

Interestingly, no significant differences in *Claudin-5* expression were found between PBCEC and PBCEC treated with Tunicamycin (mean difference = 0.55, adjusted $p = 0.9806$), between PBCEC & T10 and PBCEC & T10 Tunicamycin (mean difference = 0.32, adjusted $p = 0.9983$), or between PBCEC & U87 and PBCEC & U87 Tunicamycin (mean difference = 1.43, adjusted $p = 0.4902$). These findings indicate that Tunicamycin treatment did not alter Claudin-5 expression in either glioma co-culture model.

Furthermore, no statistically significant differences were observed in *ZO-1* or *MFSD2A* expression between untreated and Tunicamycin-treated conditions (all adjusted $p > 0.05$).

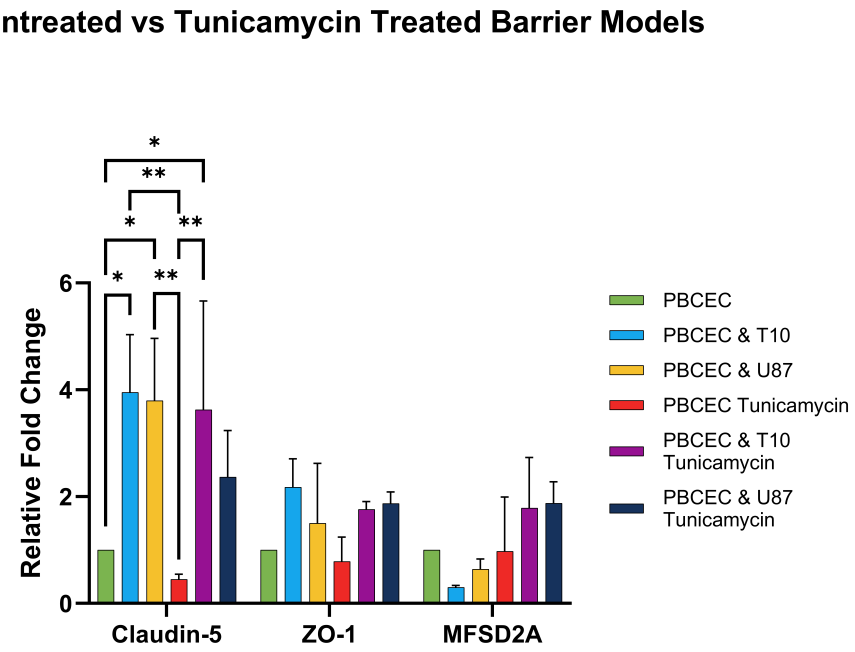

Figure 9: Relative mRNA expression of *Claudin-5*, *ZO-1*, and *MFSD2A* in untreated and tunicamycin-treated BBB and BBTB in vitro models. Porcine brain capillary endothelial cells (PBCEC) represent the BBB model, while PBCEC & T10 and PBCEC & U87 represent BBTB models. Tunicamycin-treated conditions are indicated for each model. Each bar shows the mean relative expression (normalised to PBCEC) from two biological replicates ($n = 2$), where each replicate was generated by pooling RNA from three filter inserts. *Claudin-5* expression was significantly upregulated in PBCEC & T10 (*, $p < 0.05$), PBCEC & U87 (*, $p < 0.05$), and PBCEC & T10 Tunicamycin (*, $p < 0.05$) compared to PBCEC. Additionally, *Claudin-5* expression in PBCEC Tunicamycin was significantly lower than in PBCEC & T10 (**,$p < 0.01$), PBCEC & U87 (**,$p < 0.01$), and PBCEC & T10 Tunicamycin (**,$p < 0.01$). No significant differences were observed in *ZO-1* or *MFSD2A* expression between untreated and tunicamycin-treated conditions. Data are presented as mean ± SEM. Statistical analysis was performed using 2-way ANOVA followed by Tukey's multiple comparisons test. Asterisks indicate significance levels: * $p < 0.05$, ** $p < 0.01$.

7.2.2 Expression after Metoclopramide treatment

To evaluate whether Metoclopramide treatment affects endothelial gene expression, the expression levels of *Claudin-5*, *ZO-1*, and *CD93* were analysed in BBB and BBTB in vitro models (Figure 10). Each condition was represented by two biological replicates, with RNA pooled from three filter inserts per replicate.

Claudin-5 expression was significantly lower in PBCEC treated with Metoclopramide compared to PBCEC & T10 (mean difference = -2.953, $p = 0.0140$) and PBCEC & U87 (mean difference = -2.796, $p = 0.0214$). A significant reduction was also observed in PBCEC & T10 treated with Metoclopramide compared to its untreated counterpart (mean difference = -2.937, $p = 0.0147$), and compared to PBCEC & U87 (mean difference = -2.779, $p = 0.0223$). No significant difference was found between treated and untreated PBCEC & U87 (mean difference = -0.8803, $p = 0.8613$), nor between PBCEC & T10 Metoclopramide and PBCEC & U87 Metoclopramide (mean difference = -0.8499, $p = 0.8775$). Additionally, Claudin-5 expression in PBCEC treated with Metoclopramide did not differ significantly from untreated PBCEC (mean difference = -0.6767, $p = 0.9487$).

CD93 expression was analysed to determine whether Metoclopramide treatment affected its levels in BBB and BBTB models. No statistically significant differences were observed between treated and untreated conditions in any of the three core models. Specifically, CD93 expression in PBCEC treated with Metoclopramide did not differ significantly from untreated PBCEC (mean difference = -0.6767, $p = 0.9487$). Similarly, no significant change was found between treated and untreated PBCEC & T10 (mean difference = -1.318, $p = 0.5509$), or between treated and untreated PBCEC & U87 (mean difference = -0.8803, $p = 0.8613$). However, CD93 expression was significantly higher in PBCEC & U87 treated with Metoclopramide compared to PBCEC (mean difference = -2.575, $p = 0.0381$), and also significantly higher than in PBCEC & T10 treated with Metoclopramide (mean difference = -2.596, $p = 0.0361$).

ZO-1 expression did not show any statistically significant differences between treated and untreated conditions across all models (all $p > 0.44$).

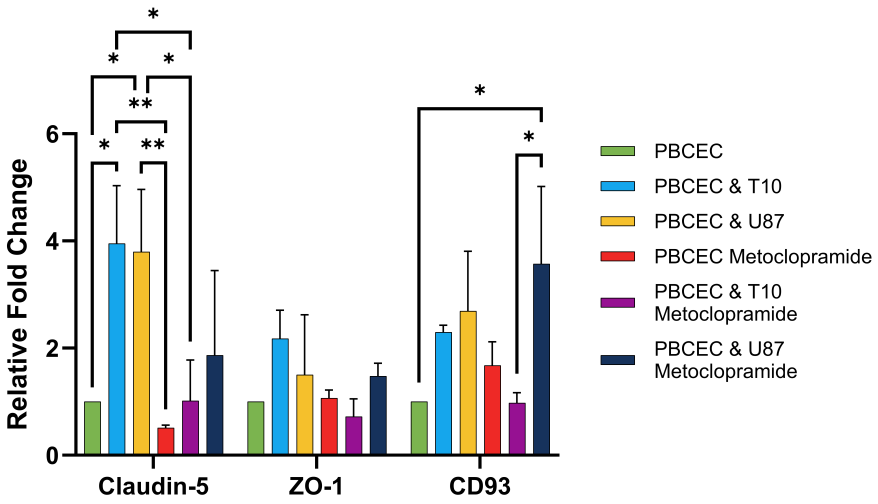

Figure 10: Relative mRNA expression of *Claudin-5*, *ZO-1*, and *CD93* in untreated and metoclopramide-treated BBB and BBTB in vitro models. Porcine brain capillary endothelial cells (PBCEC) represent the BBB model, while PBCEC & T10 and PBCEC & U87 represent BBTB models. Metoclopramide-treated conditions are indicated for each model. Each bar shows the mean relative expression (normalized to PBCEC) from two biological replicates ($n = 2$), where each replicate was generated by pooling RNA from three filter inserts. *Claudin-5* expression was significantly lower in PBCEC Metoclopramide compared to PBCEC & T10 (**,$p < 0.01$) and PBCEC & U87 (**,$p < 0.01$). PBCEC & T10 Metoclopramide showed significantly lower *Claudin-5* expression than PBCEC & T10 (*,$p < 0.05$) and PBCEC & U87 (*,$p < 0.05$). *CD93* expression was significantly higher in PBCEC & U87 Metoclopramide compared to PBCEC (*,$p < 0.05$), and also significantly higher than in PBCEC & T10 Metoclopramide (*,$p < 0.05$). No significant differences were observed in *ZO-1* expression. Data are presented as mean ± SEM. Statistical analysis was performed using 2-way ANOVA followed by Tukey's multiple comparisons test. Asterisks indicate significance levels: * $p < 0.05$, ** $p < 0.01$.

7.2.3 Expression of *CD93* & *MFSD2A* in Astrocytes & GBM-Associated Cells

To determine whether *CD93* and *MFSD2A* are expressed in astrocytes and glioblastoma-associated cells, RT-qPCR was performed on primary porcine astrocytes, as well as on T10 and U87 human GBM cell lines. Despite successful RNA extraction and cDNA synthesis, no amplification was observed for either *CD93* or *MFSD2A* in any of the tested cell types (data not shown).

7.3 Protein Expression of BBB and BBTB Models

To compare Claudin-5 protein levels between the BBB and BBTB models, PBCECs were cultured either alone or in co-culture with relevant cell types. The BBB model included PBCECs in both monoculture and co-culture with primary astrocytes, thereby representing a physiological brain microenvironment. The BBTB models consisted of PBCECs co-cultured with either T10 or U87 glioblastoma-associated cells, simulating tumour-associated conditions (Figure 11). Protein levels were quantified and normalised to the PBCEC monoculture. Each condition was

represented by two biological replicates, with three filter inserts pooled per replicate to ensure sufficient material for analysis.

Claudin-5 expression was significantly upregulated in PBCECs co-cultured with T10 glioma cells compared to the PBCEC monoculture. The mean fold change in the PBCEC & T10 group was 2.93, nearly three times higher than the control ($p = 0.0006$). A moderate but significant increase was also observed in the PBCEC & U87 group (mean fold change = 1.74, $p = 0.0210$). In contrast, co-culture with primary astrocytes (PBCEC & Astrocyte) did not significantly alter Claudin-5 expression relative to the control ($p = 0.1182$).

When comparing the BBTB models directly, Claudin-5 expression in the PBCEC & T10 group was significantly higher than in both the PBCEC & U87 ($p = 0.0038$) and PBCEC & Astrocyte ($p = 0.0016$) groups. No significant difference was observed between PBCEC & U87 and PBCEC & Astrocyte ($p = 0.2622$), suggesting that the T10 glioma cells exert a more pronounced effect on Claudin-5 expression than U87 cells.

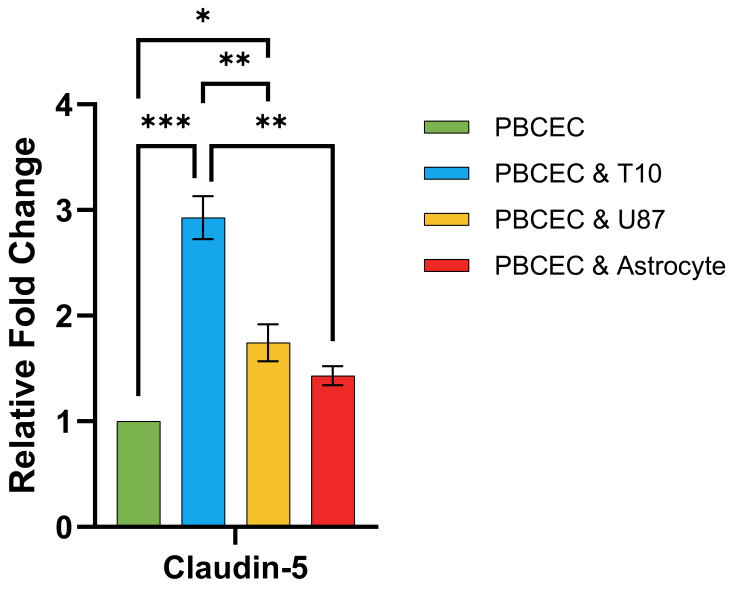

Figure 11: Relative Claudin-5 protein expression in PBCECs cultured under BBB and BBTB conditions. Each bar represents the mean fold change in Claudin-5 protein levels compared to PBCEC monoculture (set to 1.00), as determined by quantitative Western blot analysis. The BBB model includes PBCECs in monoculture and co-culture with primary astrocytes, while the BBTB models consist of co-cultures with either T10 or U87 glioblastoma-associated cells. Claudin-5 expression is significantly increased in PBCECs co-cultured with T10 and U87 cells, with the T10 condition showing the highest upregulation. No significant change was observed in the astrocyte co-culture. Statistical significance was determined by one-way ANOVA followed by Tukey's multiple comparisons test. $^*p < 0.05$, $^{**}p < 0.01$, $^{***}p < 0.001$. Data are presented as mean ± SD ($n = 2$ per group, pooled from three filter inserts).

7.3.1 Expression after Tunicamycin treatment

To explore whether inhibition of MFSD2A affects Claudin-5 protein expression, PBCECs were treated with Tunicamycin under both BBB and BBTB conditions. The experimental groups included untreated and Tunicamycin-treated PBCECs in monoculture, as well as co-cultures with T10 or U87 GBM-associated. Claudin-5 protein levels were quantified and normalised to the untreated PBCEC monoculture. Each condition was represented by two biological replicates, with three filter inserts pooled per replicate.

Claudin-5 expression was significantly higher in the PBCEC & T10 group compared to PBCEC alone ($p = 0.0384$), and this difference remained significant after Tunicamycin treatment ($p = 0.0092$). Additionally, PBCEC & T10 Tunicamycin showed significantly higher Claudin-5 expression than PBCEC treated with Tunicamycin alone ($p = 0.0092$). No significant differences were observed between PBCEC and PBCEC Tunicamycin, nor between PBCEC & U87 and its Tunicamycin-treated counterpart ($p > 0.05$ for both). These findings indicate that Tunicamycin treatment did not consistently reduce Claudin-5 expression across models, and that co-culture with T10 cells maintained elevated expression levels regardless of treatment (Figure 12).

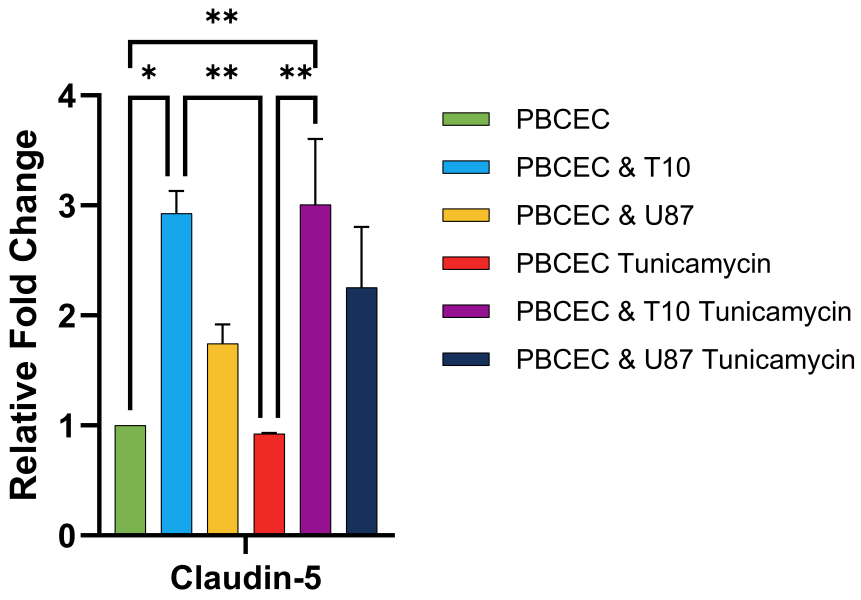

Figure 12: Relative Claudin-5 protein expression in PBCECs under untreated and Tunicamycin-treated conditions. Each bar represents the mean fold change in Claudin-5 protein levels compared to untreated PBCEC monoculture (set to 1.00), as determined by quantitative Western blot analysis. Tunicamycin was used to inhibit MFSD2A. The experimental groups include PBCECs in monoculture and co-culture with either T10 or U87 glioma cells, with or without Tunicamycin treatment. Claudin-5 expression was significantly higher in PBCEC & T10 and PBCEC & T10 + Tunicamycin compared to both PBCEC and PBCEC + Tunicamycin. Data are presented as mean ± SD ($n = 2$ per group, pooled from three filter inserts). $^*p < 0.05$, $^{**}p < 0.01$, $^{***}p < 0.001$.

7.3.2 Expression after Metoclopramide treatment

To assess whether inhibition of CD93 affects Claudin-5 protein expression, PBCECs were treated with Metoclopramide under both BBB and BBTB conditions. The experimental groups included untreated and Metoclopramide-treated PBCECs in monoculture, as well as co-cultures with T10 or U87 GBM-associated cells. Claudin-5 protein levels were quantified and normalised to the untreated PBCEC monoculture. Each condition was represented by two biological replicates, with three filter inserts pooled per replicate.

Claudin-5 expression in PBCEC & T10 Metoclopramide was significantly higher than in PBCEC ($p = 0.0341$) and PBCEC Metoclopramide ($p = 0.0373$), as shown in Figure 13. No significant difference was observed between PBCEC and PBCEC & T10 ($p = 0.3875$), nor between PBCEC and PBCEC Metoclopramide ($p > 0.9999$). Additionally, Claudin-5 levels in PBCEC & U87 and PBCEC & U87 Metoclopramide did not differ significantly ($p = 0.0809$). These results indicate that Metoclopramide treatment did not reduce Claudin-5 expression in any of the tested conditions.

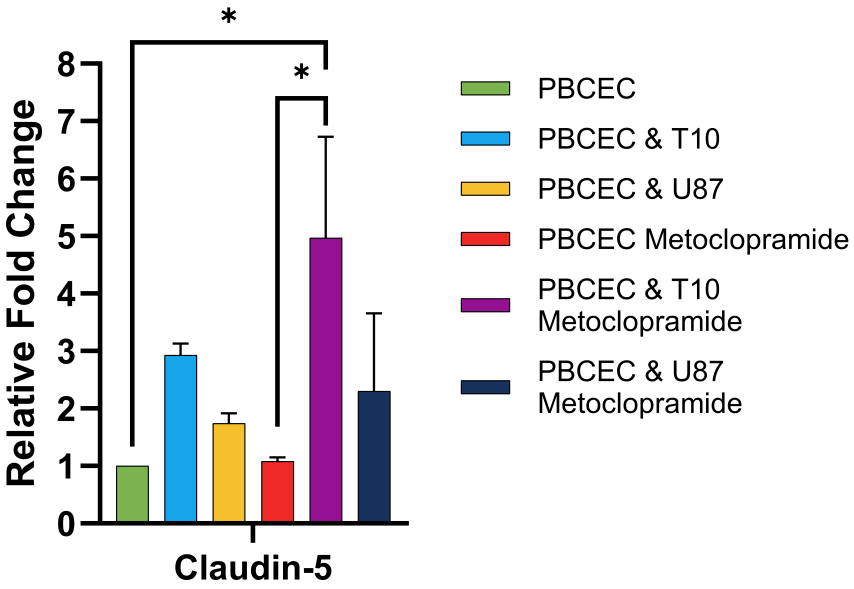

Figure 13: Relative Claudin-5 protein expression in PBCECs under untreated and Metoclopramide-treated conditions. Each bar represents the mean fold change in Claudin-5 protein levels compared to untreated PBCEC monoculture (set to 1.00), as determined by quantitative Western blot analysis. Metoclopramide was used to inhibit CD93. The experimental groups include PBCECs in monoculture and co-culture with either T10 or U87 gliomablastoma-associated cells, with or without Metoclopramide treatment. Claudin-5 expression was significantly higher in PBCEC & T10 + Metoclopramide compared to PBCEC and PBCEC + Metoclopramide. Data are presented as mean ± SD ($n = 2$ per group, pooled from three filter inserts). $^{*}p < 0.05$, $^{**}p < 0.01$, $^{***}p < 0.001$.

8 Discussion

The primary aim of this study was to investigate how glioblastoma-associated cells influence the integrity of the BBB and the BBTB, with particular focus on the expression and function of Claudin-5, ZO-1, CD93, and MFSD2A. Based on the literature, it was hypothesised that glioblastoma disrupts the BBB by downregulating tight junction proteins, thereby increasing paracellular permeability [Watkins et al., 2014, Steeg, 2021]. Furthermore, it was hypothesised that CD93 and MFSD2A expression correlate with BBTB integrity, with CD93 promoting vascular permeability [Barbera et al., 2021] and MFSD2A supporting tight junction stability and suppressing transcytosis [Ocak et al., 2020]. However, the results obtained in this study challenge both hypotheses and instead suggest a more complex and context-dependent interaction between glioblastoma cells and endothelial barrier function.

Initial TEER measurements revealed a consistent and substantial increase in barrier integrity in the PBCEC & T10 co-culture model compared to both U87 and astrocyte co-cultures. By Day 9, PBCEC & T10 displayed the highest TEER values, exceeding those of PBCEC & U87 by $238.2 \pm 211.97\ \Omega \cdot \mathrm{cm}^2$ ($p = 0.0006$) and PBCEC & Astrocyte by $371.6 \pm 181.21\ \Omega \cdot \mathrm{cm}^2$ ($p < 0.0001$). In contrast, the PBCEC & U87 model exhibited a more modest elevation ($212.3 \pm 127.69\ \Omega \cdot \mathrm{cm}^2$, $p = 0.0028$) relative to monoculture, while PBCEC & Astrocyte showed only a slight increase ($78.9 \pm 64.95\ \Omega \cdot \mathrm{cm}^2$, $p = 0.0023$). These patterns suggest that glioblastoma cells, particularly those of the T10 line, can significantly enhance barrier properties compared to both malignant and non-malignant brain-associated cell types.

Together, these findings suggest that glioblastoma-associated cells, particularly the newer patient-derived T10 line, were observed, within a 9-day co-culture period, to reinforce junctional stability and elevate TEER. This reinforcement is not only reflected in TEER measurements but is supported by the molecular data, with untreated PBCEC & T10 cultures showing a 2.95-fold increase in Claudin-5 mRNA expression and a 2.93-fold elevation at the protein level compared to PBCEC monoculture. At the same time, MFSD2A and CD93 transcripts remained essentially unchanged. The sustained upregulation of Claudin-5 suggests that glioblastoma-associated barrier reinforcement may be mediated, at least in part, through transcriptional and translational control of tight junction proteins. Whether this reinforcement would persist, plateau, or decline over an extended period remains unknown. The TEER and Claudin-5 elevation observed here may represent an early phase in glioma–endothelial interactions, after which the balance of signalling could shift. Prolonged culture might reveal a gradual loss of reinforcement if destabilising influences accumulate, or conversely, a sustained high-barrier state if the reinforcing factors remain dominant. Without longitudinal data beyond Day 9, the trajectory of these effects can only be speculated upon, underscoring the need for extended time-course experiments to capture the whole evolution of BBTB behaviour in these models.

The discrepancy between U87 and T10 highlights the importance of cell line selection in glioblastoma research. U87 is a widely used glioblastoma cell line, initially derived in 1966. Still, it has undergone extensive passaging, leading to chromosomal aberrations and altered gene expression profiles that diverge from the original tumour phenotype [Allen et al., 2016, Pokorná et al., 2021]. These changes may explain the relatively modest TEER

increase and Claudin-5 upregulation observed in the PBCEC & U87 co-culture. In contrast, T10 is a more recently established cell line derived from a Danish patient in 2019 and maintained at low passage numbers. It is presumed to retain many of the original tumour's molecular features [Torsvik et al., 2014], which may account for the pronounced reinforcement of barrier properties, including the highest TEER values and Claudin-5 protein expression, observed in the PBCEC & T10 model.

The astrocyte co-culture model was included as a non-malignant reference to determine whether the barrier reinforcement observed in glioblastoma co-cultures represented a general property of glia–endothelial interactions or a tumour-specific phenomenon. Astrocytes are a key cellular component of the neurovascular unit. They are well established as regulators of BBB stability under physiological conditions, in part through the secretion of soluble factors, including VEGF, TGF-β, and Wnt ligands, as well as through contact-mediated signalling at astrocytic endfeet [Abbott et al., 2006b, Michinaga and Koyama, 2019, Schiera et al., 2024]. In healthy brain tissue, these signals help maintain tight junction integrity, suppress transcytosis, and regulate the expression of endothelial transporters [Abbott et al., 2006b, Michinaga and Koyama, 2019, Schiera et al., 2024]. In this study, PBCEC & Astrocyte co-cultures exhibited only a modest TEER increase compared to monoculture, substantially lower than that seen in either glioblastoma model. This disparity suggests that while astrocyte-derived cues contribute to barrier stability, the degree of reinforcement observed in PBCEC & T10 — and to a lesser extent PBCEC & U87 — is unlikely to result from generic glial support alone. It should also be noted that the present model lacks pericytes, another essential component of the neurovascular unit, which is known to play a crucial role in the development and maintenance of the BBB. Their absence may have influenced the magnitude or characteristics of the barrier responses observed, and future models incorporating pericytes could provide a more physiologically representative assessment of glioma–endothelial interactions.

Tunicamycin, an inhibitor of N-linked glycosylation known to impair MFSD2A function and promote transcytosis Xu et al. [2024], was applied to the PBCEC & T10 co-culture. Between Day 7 and Day 8, before drug administration, TEER decreased by 70.3 $\pm$ 27.8 $\Omega{\cdot}\text{cm}^2$ ($p = 0.0272$), indicating a modest spontaneous decline. Following Tunicamycin treatment at Day 8, TEER decreased by 102.2 $\pm$ 39.9 $\Omega{\cdot}\text{cm}^2$ ($p = 0.0134$) between Day 8 and Day 9. Although the post-treatment decline was slightly greater ($\sim$32 $\Omega{\cdot}\text{cm}^2$ difference), the change was modest, suggesting that MFSD2A inhibition exerted only a limited additional effect on barrier integrity under these conditions. As mentioned earlier, TEER measurements can be influenced by experimental variability, including differences in cell proliferation, maturation, or confluence between inserts, all of which can change baseline values and the rate of change.

At the transcriptional level, Claudin-5 expression in Tunicamycin-treated PBCEC & T10 cultures was only slightly higher than in the untreated PBCEC & T10 condition (+0.33-fold difference), and MFSD2A expression likewise remained unchanged. Protein quantification showed a similar pattern, with Tunicamycin-treated PBCEC & T10 cultures having only a +0.08-fold higher Claudin-5 abundance than the untreated condition. This minimal change suggests that glioblastoma-derived signals, particularly from the T10 line, could override the expected effects of MFSD2A inhibition by maintaining a pro-barrier transcriptional program through alternative signalling pathways. Such compensatory mechanisms might involve persistent activation of endothelial stabilising cues,

including upregulation of other tight junction regulators or modulation of cytoskeletal architecture, which could sustain Claudin-5 levels independently of MFSD2A. Another possibility is that the MFSD2A function was already attenuated or functionally bypassed in the co-culture context, meaning that pharmacological inhibition with Tunicamycin produced minimal additional effect. Glioma cells may also influence post-translational modifications or trafficking of junctional proteins in a manner that renders the barrier less dependent on MFSD2A-mediated suppression of transcytosis.

Metoclopramide, an antagonist of dopamine D_2 receptors and reported inhibitor of CD93 signalling Riether et al. [2021], was applied to PBCEC & T10 and PBCEC & U87 co-cultures at Day 8. Between Day 7 and Day 8, before treatment, TEER increased by 36.5 ± X $\Omega \cdot cm^2$ in PBCEC & T10 and showed minimal change in PBCEC & U87, indicating stable or slightly rising barrier integrity before drug administration. Following Metoclopramide treatment, TEER in PBCEC & T10 increased by only 0.5 ± X $\Omega \cdot cm^2$ between Day 8 and Day 9, representing a marked reduction in the rate of TEER gain compared with the pre-treatment interval. PBCEC & U87 likewise exhibited minimal post-treatment change. As noted earlier, TEER measurements can be influenced by subtle experimental variability, including slight differences in insert seeding density, cell distribution, and handling during drug application, which may contribute to the modest magnitude of these changes.

At the mRNA level, Claudin-5 expression in Metoclopramide-treated PBCEC & T10 cultures was lower than in the untreated PBCEC & T10 condition (2.9-fold vs. untreated baseline), and PBCEC & U87 cultures showed a similar reduction (1.9-fold vs. untreated baseline). Protein quantification, however, revealed the opposite trend: Claudin-5 abundance in Metoclopramide-treated PBCEC & T10 cultures was 2.04-fold higher than in the untreated condition, and PBCEC & U87 showed a 0.56-fold increase. This discrepancy between transcriptional and protein-level responses may arise from biological variation between the pooled inserts used for mRNA and protein quantification. Even with identical seeding densities and culture conditions, slight differences in PBCEC proliferation, maturation, or confluence can influence Claudin-5 expression, potentially leading to higher protein abundance in the inserts used for protein extraction compared to those used for RNA isolation. Such variation is consistent with the TEER measurements, which also showed noticeable differences between inserts. Alternatively, genuine post-transcriptional mechanisms, altered protein stability, or changes in intracellular trafficking could sustain Claudin-5 abundance despite reduced mRNA levels. In either case, the lack of a substantial TEER decrease following treatment supports the idea that other junctional components or redundant signalling pathways can uphold barrier integrity when Claudin-5 transcription is suppressed. Additionally, glioblastoma-derived paracrine factors in the co-culture environment may maintain a pro-barrier phenotype independently of CD93-mediated signalling, thereby mitigating the functional impact of its inhibition.

Taken together, these results suggest that the barrier-enhancing effect of glioblastoma cells, particularly T10, is resilient to pharmacological disruption of MFSD2A and CD93 signalling. This resilience may reflect compensatory mechanisms within the endothelial cells or a dominant paracrine influence from the glioblastoma cells that overrides the inhibitory effects of the drugs. Another possibility is that the inhibitors used in this study did not achieve sufficient intracellular concentrations to engage their targets fully. Brain endothelial cells express high levels of ATP-binding cassette (ABC) transporters, including P-glycoprotein and breast cancer resistance protein

(BCRP), which actively export a wide range of xenobiotics. If Tunicamycin or Metoclopramide are substrates for these transporters, they may have been rapidly removed from the cells, limiting their bioavailability. In addition, the concentrations used here, 1 μg/mL for Tunicamycin and 1 μM for Metoclopramide, may have been insufficient to overcome active efflux or achieve complete target inhibition. Together, these factors could partially explain the limited impact observed at both the functional level, as measured by TEER, and the molecular level, as reflected in the expression of Claudin-5, ZO-1, MFSD2A, and CD93.

This raises important considerations for the therapeutic targeting of BBTB integrity. In glioblastoma, the optimal strategy is not necessarily straightforward: weakening the barrier could improve delivery of chemotherapeutics to the tumour core, yet such an approach could also have unintended effects on the surrounding brain microenvironment. The key challenge is whether a transient, controlled modulation of the BBTB can be achieved, allowing drug delivery when needed without long-term compromise of barrier function. Addressing this will require a detailed understanding of the specific signals that govern barrier reinforcement in the glioma microenvironment.

Given the transwell setup used in this study, direct cell–cell contact between glioblastoma cells and endothelial cells was excluded, meaning that the observed barrier reinforcement must have been mediated entirely through paracrine signalling. This design choice is important because it isolates the effects of secreted mediators such as cytokines, growth factors, and extracellular vesicles from those that require physical interaction, such as adhesion molecule engagement or mechanotransduction. Consequently, the results demonstrate that direct contact is not necessary for glioblastoma cells, particularly the T10 line, to induce pronounced barrier strengthening. However, this also means that any contact-dependent mechanisms that might occur in vivo were not captured here, and the overall magnitude or nature of barrier modulation in a more physiologically integrated environment could differ. The persistence of reinforcement despite single-target inhibition in this setup suggests that glioblastoma cells secrete multiple, potentially redundant, factors converging on tight junction regulation, which could help explain the limited drug effects observed.

One promising avenue for future research is the role of extracellular vesicles (EVs), which can carry proteins, RNAs, and lipids that influence endothelial phenotype Schiera et al. [2024]. The upregulation of Claudin-5 and CD93 in response to glioma co-culture suggests that EVs from T10 and U87 cells may contain cargo that promotes junctional stability. Future studies should isolate and characterise EVs from these cell lines to identify specific mediators of barrier modulation. Such work could also investigate whether EV-mediated reinforcement is more pronounced in patient-derived models, such as T10, compared to established lines like U87.

The reinforcement of endothelial barrier properties by glioblastoma cells may contribute to the well-documented therapeutic resistance of glioblastoma. Regions of the tumour with intact or reinforced BBTB may hinder the penetration of chemotherapeutic agents, limiting their efficacy Steeg [2021]. Understanding the molecular mechanisms behind this reinforcement could inform the development of strategies to transiently modulate the BBTB, enhancing drug delivery without compromising overall BBB function. It is also possible that glioblastoma cells exploit barrier reinforcement as a means of immune evasion, limiting the infiltration of cytotoxic T cells or therapeutic antibodies. The dual role of the BBTB as both a physical and immunological barrier warrants further investigation.

8.1 Conclusion

The findings presented in this thesis contest the traditional paradigm that glioblastoma universally compromises the integrity of the blood–brain barrier (BBB). Instead, within a 9-day co-culture period, the data reveal a context-dependent modulation of endothelial barrier properties, in which glioblastoma-associated cells, particularly the patient-derived T10 line, can reinforce junctional stability and increase transendothelial electrical resistance (TEER). This phenomenon was observed across various experimental modalities, including gene and protein expression analyses, and persisted despite pharmacological inhibition of CD93 and MFSD2A.

These results emphasise the intricate nature of glioma–endothelial interactions and highlight the limitations of overly simplified models of blood–brain tumour barrier (BBTB) disruption. The distinct behaviours observed in the T10 and U87 cell lines underscore the significance of tumour heterogeneity and cell line provenance in experimental glioblastoma studies. Furthermore, the modest barrier reinforcement seen in astrocyte co-cultures, relative to either glioblastoma model, suggests that tumour-derived signalling exerts a dominant influence over BBTB modulation in this in vitro context. It should be noted, however, that the absence of pericytes in the present model may have influenced the magnitude and characteristics of the barrier effects observed.

From a translational perspective, the reinforcement of the BBTB poses a significant obstacle to effective drug delivery, particularly in infiltrative tumour regions where the barrier remains functionally intact. These findings advocate for the development of targeted strategies to transiently modulate barrier properties without compromising overall BBB function. Future studies should prioritise the characterisation of glioma-derived extracellular vesicles, the identification of stabilising molecular cargo, and the exploration of combinatorial approaches to overcome pharmacological resistance.

In summary, this thesis contributes to a more nuanced understanding of BBTB biology in glioblastoma and provides a foundation for future investigations into barrier-targeted therapeutic interventions. By elucidating the mechanisms of barrier reinforcement, this research paves the way for novel advancements in drug delivery and therapeutic efficacy, particularly in one of the most treatment-resistant forms of brain cancer. The findings presented in this thesis contest the traditional paradigm that glioblastoma universally compromises the integrity of the blood–brain barrier (BBB). Instead, the data indicate a context-dependent modulation of the endothelial barrier, wherein glioblastoma-associated cells—particularly the patient-derived T10 line—may reinforce junctional stability and increase transendothelial electrical resistance (TEER). This phenomenon was observed across various experimental modalities, including gene and protein expression analyses, and persisted despite pharmacological inhibition of CD93 and MFSD2A.

References

Freddie Bray, Mathieu Laversanne, Hyuna Sung, Jacques Ferlay, Rebecca L. Siegel, Isabelle Soerjomataram, and Ahmedin Jemal. Global cancer statistics 2022: Globocan estimates of incidence and mortality worldwide for 36 cancers in 185 countries. *CA: A Cancer Journal for Clinicians*, 74:229–263, 5 2024. ISSN 1542-4863. doi: 10.3322/CAAC.21834.

Danmarks-Statistik. Dødsfald - danmarks statistik, 2024. URL `https://www.dst.dk/da/Statistik/emner/borgere/befolkning/doedsfald`.

Lauren R. Schaff and Ingo K. Mellinghoff. Glioblastoma and other primary brain malignancies in adults: A review. *JAMA*, 329:574–587, 2 2023. ISSN 0098-7484. doi: 10.1001/JAMA.2023.0023.

Quinn T. Ostrom, Mackenzie Price, Katherine Ryan, Jacob Edelson, Corey Neff, Gino Cioffi, Kristin A. Waite, Carol Kruchko, and Jill S. Barnholtz-Sloan. Cbtrus statistical report: Pediatric brain tumor foundation childhood and adolescent primary brain and other central nervous system tumors diagnosed in the united states in 2014–2018. *Neuro-Oncology*, 24:iii1–iii38, 9 2022. ISSN 1522-8517. doi: 10.1093/NEUONC/NOAC161.

David N. Louis, Arie Perry, Pieter Wesseling, Daniel J. Brat, Ian A. Cree, Dominique Figarella-Branger, Cynthia Hawkins, H. K. Ng, Stefan M. Pfister, Guido Reifenberger, Riccardo Soffietti, Andreas Von Deimling, and David W. Ellison. The 2021 who classification of tumors of the central nervous system: a summary. *Neuro-Oncology*, 23:1231–1251, 8 2021. ISSN 1522-8517. doi: 10.1093/NEUONC/NOAB106.

Szymon Grochans, Anna Maria Cybulska, Donata Simińska, Jan Korbecki, Klaudyna Kojder, Dariusz Chlubek, and Irena Baranowska-Bosiacka. Epidemiology of glioblastoma multiforme–literature review. *Cancers*, 14:2412, 5 2022. ISSN 20726694. doi: 10.3390/CANCERS14102412.

Steinbjørn Hansen, Birthe Krogh Rasmussen, René Johannes Laursen, Michael Kosteljanetz, Henrik Schultz, Bente Mertz Nørgård, Rikke Guldberg, and Kim Oren Gradel. Treatment and survival of glioblastoma patients in denmark: The danish neuro-oncology registry 2009–2014. *Journal of Neuro-Oncology*, 139:479–489, 9 2018. ISSN 15737373. doi: 10.1007/S11060-018-2892-7/TABLES/4.

Sverre Helge Torp, Ole Solheim, and Anne Jarstein Skjulsvik. The who 2021 classification of central nervous system tumours: a practical update on what neurosurgeons need to know—a minireview. *Acta Neurochirurgica*, 164: 2453, 9 2022. ISSN 09420940. doi: 10.1007/S00701-022-05301-Y.

Alba Loras, Luis G. Gonzalez-Bonet, Julia L. Gutierrez-Arroyo, Conrado Martinez-Cadenas, and Maria Angeles Marques-Torrejon. Neural stem cells as potential glioblastoma cells of origin. *Life*, 13:905, 4 2023. ISSN 20751729. doi: 10.3390/LIFE13040905.

Jamison Beiriger, Ahmed Habib, Nicolina Jovanovich, Chowdari V. Kodavali, Lincoln Edwards, Nduka Amankulor, and Pascal O. Zinn. The subventricular zone in glioblastoma: Genesis, maintenance, and modeling. *Frontiers in Oncology*, 12:790976, 3 2022. ISSN 2234943X. doi: 10.3389/FONC.2022.790976/BIBTEX.

Elena Verdugo, Iker Puerto, and Miguel Ángel Medina. An update on the molecular biology of glioblastoma, with clinical implications and progress in its treatment. *Cancer Communications*, 42:1083–1111, 11 2022. ISSN 25233548. doi: 10.1002/cac2.12361.

Qianghu Wang, Baoli Hu, Xin Hu, Hoon Kim, Massimo Squatrito, Lisa Scarpace, Ana C. deCarvalho, Sali Lyu, Pengping Li, Yan Li, Floris Barthel, Hee Jin Cho, Yu Hsi Lin, Nikunj Satani, Emmanuel Martinez-Ledesma, Siyuan Zheng, Edward Chang, Charles Etienne Gabriel Sauvé, Adriana Olar, Zheng D. Lan, Gaetano Finocchiaro, Joanna J. Phillips, Mitchel S. Berger, Konrad R. Gabrusiewicz, Guocan Wang, Eskil Eskilsson, Jian Hu, Tom Mikkelsen, Ronald A. DePinho, Florian Muller, Amy B. Heimberger, Erik P. Sulman, Do Hyun Nam, and Roel G.W. Verhaak. Tumor evolution of glioma intrinsic gene expression subtype associates with immunological changes in the microenvironment. *Cancer cell*, 32:42, 7 2017. ISSN 18783686. doi: 10.1016/J.CCELL.2017.06.003.

Roel G.W. Verhaak, Katherine A. Hoadley, Elizabeth Purdom, Victoria Wang, Yuan Qi, Matthew D. Wilkerson, C. Ryan Miller, Li Ding, Todd Golub, Jill P. Mesirov, Gabriele Alexe, Michael Lawrence, Michael O'Kelly, Pablo Tamayo, Barbara A. Weir, Stacey Gabriel, Wendy Winckler, Supriya Gupta, Lakshmi Jakkula, Heidi S. Feiler, J. Graeme Hodgson, C. David James, Jann N. Sarkaria, Cameron Brennan, Ari Kahn, Paul T. Spellman, Richard K. Wilson, Terence P. Speed, Joe W. Gray, Matthew Meyerson, Gad Getz, Charles M. Perou, and D. Neil Hayes. An integrated genomic analysis identifies clinically relevant subtypes of glioblastoma characterized by abnormalities in pdgfra, idh1, egfr and nf1. *Cancer cell*, 17:98, 1 2010. ISSN 15356108. doi: 10.1016/J.CCR.2009.12.020.

Filippo Torrisi, Cristiana Alberghina, Simona D'aprile, Anna M. Pavone, Lucia Longhitano, Sebastiano Giallongo, Daniele Tibullo, Michelino Di Rosa, Agata Zappalà, Francesco P. Cammarata, Giorgio Russo, Massimo Ippolito, Giacomo Cuttone, Giovanni Li Volti, Nunzio Vicario, and Rosalba Parenti. The hallmarks of glioblastoma: Heterogeneity, intercellular crosstalk and molecular signature of invasiveness and progression. *Biomedicines*, 10, 4 2022. ISSN 22279059. doi: 10.3390/biomedicines10040806.

Patrick Y. Wen, Michael Weller, Eudocia Quant Lee, Brian M. Alexander, Jill S. Barnholtz-Sloan, Floris P. Barthel, Tracy T. Batchelor, Ranjit S. Bindra, Susan M. Chang, E. Antonio Chiocca, Timothy F. Cloughesy, John F. DeGroot, Evanthia Galanis, Mark R. Gilbert, Monika E. Hegi, Craig Horbinski, Raymond Y. Huang, Andrew B. Lassman, Emilie Le Rhun, Michael Lim, Minesh P. Mehta, Ingo K. Mellinghoff, Giuseppe Minniti, David Nathanson, Michael Platten, Matthias Preusser, Patrick Roth, Marc Sanson, David Schiff, Susan C. Short, Martin J.B. Taphoorn, Joerg Christian Tonn, Jonathan Tsang, Roel G.W. Verhaak, Andreas von Deimling, Wolfgang Wick, Gelareh Zadeh, David A. Reardon, Kenneth D. Aldape, and Martin J. van den Bent.

Glioblastoma in adults: a society for neuro-oncology (sno) and european society of neuro-oncology (eano) consensus review on current management and future directions. *Neuro-Oncology*, 22:1073, 8 2020. ISSN 15235866. doi: 10.1093/NEUONC/NOAA106.

Liang Rong, Ni Li, and Zhenzhen Zhang. Emerging therapies for glioblastoma: current state and future directions. *Journal of Experimental and Clinical Cancer Research : CR*, 41:142, 12 2022. ISSN 17569966. doi: 10.1186/S13046-022-02349-7.

Wei Wu, Jessica L. Klockow, Michael Zhang, Famyrah Lafortune, Edwin Chang, Linchun Jin, Yang Wu, and Heike E. Daldrup-Link. Glioblastoma multiforme (gbm): An overview of current therapies and mechanisms of resistance. *Pharmacological research*, 171:105780, 9 2021. ISSN 10961186. doi: 10.1016/J.PHRS.2021.105780.

Mary Elizabeth Davis. Glioblastoma: Overview of disease and treatment. *Clinical journal of oncology nursing*, 20:S2, 10 2016. ISSN 1538067X. doi: 10.1188/16.CJON.S1.2-8.

Roger Stupp, Warren P. Mason, Martin J. van den Bent, Michael Weller, Barbara Fisher, Martin J.B. Taphoorn, Karl Belanger, Alba A. Brandes, Christine Marosi, Ulrich Bogdahn, Jürgen Curschmann, Robert C. Janzer, Samuel K. Ludwin, Thierry Gorlia, Anouk Allgeier, Denis Lacombe, J. Gregory Cairncross, Elizabeth Eisenhauer, and René O. Mirimanoff. Radiotherapy plus concomitant and adjuvant temozolomide for glioblastoma. *New England Journal of Medicine*, 352:987–996, 3 2005. ISSN 0028-4793. doi: 10.1056/NEJMOA043330/SUPPL_FILE/987SA1.PDF.

J. R. Wesolowski, P. Rajdev, and S. K. Mukherji. Temozolomide (temodar). *AJNR: American Journal of Neuroradiology*, 31:1383, 9 2010. ISSN 01956108. doi: 10.3174/AJNR.A2170.

Agathe L. Chédeville and Patricia A. Madureira. The role of hypoxia in glioblastoma radiotherapy resistance. *Cancers 2021, Vol. 13, Page 542*, 13:542, 2 2021. ISSN 2072-6694. doi: 10.3390/CANCERS13030542.

Hossam Kadry, Behnam Noorani, and Luca Cucullo. A blood–brain barrier overview on structure, function, impairment, and biomarkers of integrity. *Fluids and Barriers of the CNS 2020 17:1*, 17:1–24, 11 2020. ISSN 2045-8118. doi: 10.1186/S12987-020-00230-3.

Jeffrey J. Lochhead, Junzhi Yang, Patrick T. Ronaldson, and Thomas P. Davis. Structure, function, and regulation of the blood-brain barrier tight junction in central nervous system disorders. *Frontiers in Physiology*, 11:558491, 8 2020. ISSN 1664042X. doi: 10.3389/FPHYS.2020.00914/PDF.

Elisabeth C. Kugler, John Greenwood, and Ryan B. MacDonald. The "neuro-glial-vascular" unit: The role of glia in neurovascular unit formation and dysfunction. *Frontiers in Cell and Developmental Biology*, 9, 9 2021. ISSN 2296634X. doi: 10.3389/fcell.2021.732820.

Heather L. McConnell and Anusha Mishra. Cells of the blood–brain barrier: An overview of the neurovascular unit in health and disease. *Methods in Molecular Biology*, 2492:3–24, 2022. ISSN 19406029.

doi: 10.1007/978-1-0716-2289-6_1/FIGURES/5. URL https://link.springer.com/protocol/10.1007/978-1-0716-2289-6_1.

Di Wu, Qi Chen, Xiaojie Chen, Feng Han, Zhong Chen, and Yi Wang. The blood–brain barrier: Structure, regulation and drug delivery. *Signal Transduction and Targeted Therapy 2023 8:1*, 8:1–27, 5 2023. ISSN 2059-3635. doi: 10.1038/s41392-023-01481-w.

N. Joan Abbott, Adjanie A.K. Patabendige, Diana E.M. Dolman, Siti R. Yusof, and David J. Begley. Structure and function of the blood–brain barrier. *Neurobiology of Disease*, 37:13–25, 1 2010. ISSN 0969-9961. doi: 10.1016/J.NBD.2009.07.030.

Qasim Alhadidi, Muhammad Shahdaat Bin Sayeed, and Zahoor A. Shah. The interplay between cofilin and phospho-cofilin: Its role in maintaining blood brain barrier integrity. *CNS and Neurological Disorders - Drug Targets*, 16:279–290, 2 2017. ISSN 18715273. doi: 10.2174/1871527316666170117115040.

Annika Armulik, Guillem Genové, and Christer Betsholtz. Pericytes: Developmental, physiological, and pathological perspectives, problems, and promises. *Developmental Cell*, 21:193–215, 8 2011. ISSN 1534-5807. doi: 10.1016/J.DEVCEL.2011.07.001.

Ethan A. Winkler, Jesse D. Sengillo, Robert D. Bell, Joseph Wang, and Berislav V. Zlokovic. Blood–spinal cord barrier pericyte reductions contribute to increased capillary permeability. *Journal of Cerebral Blood Flow and Metabolism*, 32:1841, 10 2012. ISSN 0271678X. doi: 10.1038/JCBFM.2012.113.

Annika Armulik, Guillem Genové, Maarja Mäe, Maya H. Nisancioglu, Elisabet Wallgard, Colin Niaudet, Liqun He, Jenny Norlin, Per Lindblom, Karin Strittmatter, Bengt R. Johansson, and Christer Betsholtz. Pericytes regulate the blood–brain barrier. *Nature 2010 468:7323*, 468:557–561, 10 2010. ISSN 1476-4687. doi: 10.1038/nature09522.

Richard Daneman, Lu Zhou, Amanuel A. Kebede, and Ben A. Barres. Pericytes are required for blood–brain barrier integrity during embryogenesis. *Nature 2010 468:7323*, 468:562–566, 10 2010. ISSN 1476-4687. doi: 10.1038/nature09513.

Nicola J. Allen and Cagla Eroglu. Cell biology of astrocyte-synapse interactions. *Neuron*, 96:697, 11 2017. ISSN 10974199. doi: 10.1016/J.NEURON.2017.09.056.

Gary A. Banker. Trophic interactions between astroglial cells and hippocampal neurons in culture. *Science (New York, N.Y.)*, 209:809–810, 1980. ISSN 0036-8075. doi: 10.1126/SCIENCE.7403847.

Michael V. Sofroniew and Harry V. Vinters. Astrocytes: biology and pathology. *Acta Neuropathologica*, 119:7, 1 2009. ISSN 00016322. doi: 10.1007/S00401-009-0619-8.

N. Joan Abbott, Lars Rönnbäck, and Elisabeth Hansson. Astrocyte–endothelial interactions at the blood–brain barrier. *Nature Reviews Neuroscience 2006 7:1*, 7:41–53, 1 2006a. ISSN 1471-0048. doi: 10.1038/nrn1824.

Karen Wolburg-Buchholz, Andreas F. Mack, Esther Steiner, Friederike Pfeiffer, Britta Engelhardt, and Hartwig Wolburg. Loss of astrocyte polarity marks blood-brain barrier impairment during experimental autoimmune encephalomyelitis. *Acta Neuropathologica*, 118:219–233, 6 2009. ISSN 00016322. doi: 10.1007/S00401-009-0558-4/FIGURES/9.

Hartwig Wolburg, Karen Wolburg-Buchholz, Petra Fallier-Becker, Susan Noell, and Andreas F. Mack. Structure and functions of aquaporin-4-based orthogonal arrays of particles. *International Review of Cell and Molecular Biology*, 287:1–41, 1 2011. ISSN 1937-6448. doi: 10.1016/B978-0-12-386043-9.00001-3.

Gabriella Schiera, Carlo Maria Di Liegro, Giuseppe Schirò, Gabriele Sorbello, and Italia Di Liegro. Involvement of astrocytes in the formation, maintenance, and function of the blood–brain barrier. *Cells 2024, Vol. 13, Page 150*, 13:150, 1 2024. ISSN 2073-4409. doi: 10.3390/CELLS13020150.

Grant R.J. Gordon, Sean J. Mulligan, and Brian A. MacVicar. Astrocyte control of the cerebrovasculature. *Glia*, 55:1214–1221, 9 2007. ISSN 1098-1136. doi: 10.1002/GLIA.20543.

Anusha Mishra. Binaural blood flow control by astrocytes: listening to synapses and the vasculature. *The Journal of Physiology*, 595:1885, 3 2016. ISSN 14697793. doi: 10.1113/JP270979.

Shotaro Michinaga and Yutaka Koyama. Dual roles of astrocyte-derived factors in regulation of blood-brain barrier function after brain damage. *International Journal of Molecular Sciences*, 20:571, 2 2019. ISSN 14220067. doi: 10.3390/IJMS20030571.

Sachiko Tsukita, Hiroo Tanaka, and Atsushi Tamura. The claudins: From tight junctions to biological systems. *Trends in Biochemical Sciences*, 44:141–152, 2 2019. ISSN 0968-0004. doi: 10.1016/J.TIBS.2018.09.008.

Vina Tikiyani and Kavita Babu. Claudins in the brain: Unconventional functions in neurons. *Traffic*, 20:807–814, 11 2019. ISSN 16000854. doi: 10.1111/TRA.12685/.

Anny Claude Luissint, Cédric Artus, Fabienne Glacial, Kayathiri Ganeshamoorthy, and Pierre Olivier Couraud. Tight junctions at the blood brain barrier: Physiological architecture and disease-associated dysregulation. *Fluids and Barriers of the CNS*, 9:1–12, 11 2012. ISSN 20458118. doi: 10.1186/2045-8118-9-23/TABLES/1.

Tekehiro Nitta, Masaki Hata, Shimpei Gotoh, Yoshiteru Seo, Hiroyuki Sasaki, Nobuo Hashimoto, Mikio Furuse, and Shoichiro Tsukita. Size-selective loosening of the blood-brain barrier in claudin-5–deficient mice. *Journal of Cell Biology*, 161:653–660, 5 2003. ISSN 0021-9525. doi: 10.1083/JCB.200302070.

Caroline Menard, Madeline L. Pfau, Georgia E. Hodes, Veronika Kana, Victoria X. Wang, Sylvain Bouchard, Aki Takahashi, Meghan E. Flanigan, Hossein Aleyasin, Katherine B. Leclair, William G. Janssen, Benoit Labonté, Eric M. Parise, Zachary S. Lorsch, Sam A. Golden, Mitra Heshmati, Carol Tamminga, Gustavo Turecki, Matthew Campbell, Zahi A. Fayad, Cheuk Ying Tang, Miriam Merad, and Scott J. Russo. Social stress induces neurovascular pathology promoting depression. *Nature Neuroscience 2017 20:12*, 20:1752–1760, 11 2017. ISSN 1546-1726. doi: 10.1038/s41593-017-0010-3.

Filipa Lourenço Cardoso, Dora Brites, and Maria Alexandra Brito. Looking at the blood–brain barrier: Molecular anatomy and possible investigation approaches. *Brain Research Reviews*, 64:328–363, 9 2010. ISSN 0165-0173. doi: 10.1016/J.BRAINRESREV.2010.05.003.

Melanie D. Sweeney, Zhen Zhao, Axel Montagne, Amy R. Nelson, and Berislav V. Zlokovic. Blood-brain barrier: From physiology to disease and back. *Physiological Reviews*, 99:21, 1 2018. ISSN 15221210. doi: 10.1152/PHYSREV.00050.2017.

Brian T. Hawkins and Thomas P. Davis. The blood-brain barrier/neurovascular unit in health and disease. *Pharmacological Reviews*, 57:173–185, 6 2005. ISSN 0031-6997. doi: 10.1124/PR.57.2.4.

Jörg Piontek, Susanne M. Krug, Jonas Protze, Gerd Krause, and Michael Fromm. Molecular architecture and assembly of the tight junction backbone. *Biochimica et Biophysica Acta (BBA) - Biomembranes*, 1862:183279, 7 2020. ISSN 0005-2736. doi: 10.1016/J.BBAMEM.2020.183279.

Kazuaki Umeda, Junichi Ikenouchi, Sayaka Katahira-Tayama, Kyoko Furuse, Hiroyuki Sasaki, Mayumi Nakayama, Takeshi Matsui, Sachiko Tsukita, Mikio Furuse, and Shoichiro Tsukita. Zo-1 and zo-2 independently determine where claudins are polymerized in tight-junction strand formation. *Cell*, 126:741–754, 8 2006. ISSN 0092-8674. doi: 10.1016/J.CELL.2006.06.043.

Wei Ting Kuo, Matthew A. Odenwald, Jerrold R. Turner, and Li Zuo. Tight junction proteins occludin and zo-1 as regulators of epithelial proliferation and survival. *Annals of the New York Academy of Sciences*, 1514:21, 8 2022. ISSN 17496632. doi: 10.1111/NYAS.14798.

Svetlana M. Stamatovic, Allison M. Johnson, Richard F. Keep, and Anuska V. Andjelkovic. Junctional proteins of the blood-brain barrier: New insights into function and dysfunction. *Tissue Barriers*, 4:e1154641, 1 2016. ISSN 21688370. doi: 10.1080/21688370.2016.1154641.

Stacey Watkins, Stefanie Robel, Ian F. Kimbrough, Stephanie M. Robert, Graham Ellis-Davies, and Harald Sontheimer. Disruption of astrocyte–vascular coupling and the blood–brain barrier by invading glioma cells. *Nature Communications 2014 5:1*, 5:1–15, 6 2014. ISSN 2041-1723. doi: 10.1038/ncomms5196.

Olaf van Tellingen, Banu Yetkin-Arik, Marike C de Gooijer, Pieter Wesseling, Tom Wurdinger, and Helga E de Vries. Overcoming the blood–brain tumor barrier for effective glioblastoma treatment. *Drug Resistance Updates*, 19:1–12, 2015. doi: 10.1016/j.drup.2015.02.002.

Costas D Arvanitis, Gino B Ferraro, and Rakesh K Jain. The blood–brain barrier and blood–tumour barrier in brain tumours and metastases. *Nature Reviews Cancer*, 20(1):26–41, 2020. doi: 10.1038/s41568-019-0205-x.

Jann N. Sarkaria, Leland S. Hu, Ian F. Parney, Deanna H. Pafundi, Debra H. Brinkmann, Nadia N. Laack, Caterina Giannini, Terence C. Burns, Sani H. Kizilbash, Janice K. Laramy, Kristin R. Swanson, Timothy J. Kaufmann, Paul D. Brown, Nathalie Y.R. Agar, Evanthia Galanis, Jan C. Buckner, and William F. Elmquist.

Is the blood–brain barrier really disrupted in all glioblastomas? a critical assessment of existing clinical data. *Neuro-Oncology*, 20:184, 1 2017. ISSN 15235866. doi: 10.1093/NEUONC/NOX175.

Patricia S. Steeg. The blood–tumour barrier in cancer biology and therapy. *Nature Reviews Clinical Oncology 2021 18:11*, 18:696–714, 7 2021. ISSN 1759-4782. doi: 10.1038/s41571-021-00529-6.

Elise Langenkamp, Lihua Zhang, Roberta Lugano, and et al. Vessel abnormalization in glioblastoma: Cd93-targeted therapy normalizes the tumor vasculature. *The Journal of Clinical Investigation*, 125(7):2691–2706, 2015. doi: 10.1172/JCI77172.

Stefano Barbera, Roberta Lugano, Alessia Pedalina, Maurizio Mongiat, Annalisa Santucci, Gian Marco Tosi, Anna Dimberg, Federico Galvagni, and Maurizio Orlandini. The c-type lectin cd93 controls endothelial cell migration via activation of the rho family of small gtpases. *Matrix Biology*, 99:1–17, 5 2021. ISSN 0945-053X. doi: 10.1016/J.MATBIO.2021.05.006. URL `https://www.sciencedirect.com/science/article/abs/pii/S0945053X21000469`.

Roberta Lugano, Kalyani Vemuri, Stefano Barbera, Maurizio Orlandini, Elisabetta Dejana, Lena Claesson-Welsh, and Anna Dimberg. Cd93 maintains endothelial barrier function by limiting the phosphorylation and turnover of ve-cadherin. *FASEB Journal*, 37, 4 2023. ISSN 15306860. doi: 10.1096/fj.202201623RR.

Pinar Eser Ocak, Umut Ocak, Prativa Sherchan, Marcin Gamdzyk, Jiping Tang, and John H. Zhang. Overexpression of mfsd2a attenuates blood brain barrier dysfunction via cav-1/keap-1/nrf-2/ho-1 pathway in a rat model of surgical brain injury. *Experimental Neurology*, 326, 4 2020. ISSN 10902430. doi: 10.1016/j.expneurol.2020.113203.

Yuan Xie, Fan Yang, Liqun He, Hua Huang, Min Chao, Haiyan Cao, Yaqin Hu, Zhicheng Fan, Yaohong Zhai, Wenjian Zhao, Xian Liu, Ruozhu Zhao, Bing Xiao, Xinxin Shi, Yuancheng Luo, Jinlong Yin, Dayun Feng, Jean Philippe Hugnot, Lars Muhl, Anna Dimberg, Christer Betsholtz, Yanyu Zhang, Liang Wang, and Lei Zhang. Single-cell dissection of the human blood-brain barrier and glioma blood-tumor barrier. *Neuron*, 112:3089–3105.e7, 9 2024. ISSN 0896-6273. doi: 10.1016/J.NEURON.2024.07.026.

Markéta Pokorná, Michael Hudec, Iva Juříčková, Michael Vácha, Zdeňka Polívková, Viera Kútna, Jan Pala, Saak V. Ovsepian, Marie Černá, and Valerie Bríd O'leary. All-trans retinoic acid fosters the multifarious u87mg cell line as a model of glioblastoma. *Brain Sciences*, 11:812, 6 2021. ISSN 20763425. doi: 10.3390/BRAINSCI11060812/S1.

Marie Allen, Mia Bjerke, Hanna Edlund, Sven Nelander, and Bengt Westermark. Origin of the u87mg glioma cell line: Good news and bad news. *Science Translational Medicine*, 8, 8 2016. ISSN 19466242. doi: 10.1126/SCITRANSLMED.AAF6853,.

Anja Torsvik, Daniel Stieber, PerØyvind O. Enger, Anna Golebiewska, Anders Molven, Agnete Svendsen, Bengt Westermark, Simone P. Niclou, Thale Kristin Olsen, Martha Chekenya Enger, and Rolf Bjerkvig. U-251 revisited: genetic drift and phenotypic consequences of long-term cultures of glioblastoma cells. *Cancer Medicine*, 3:812–824, 8 2014. ISSN 2045-7634. doi: 10.1002/CAM4.219.

Xiaoju Xu, Ke Xu, Fengqiu Chen, Dehong Yu, and Xueling Wang. Mfsd2a regulates the blood-labyrinth-barrier formation and function through tight junctions and transcytosis. *Hearing Research*, 450:109048, 9 2024. ISSN 0378-5955. doi: 10.1016/J.HEARES.2024.109048.

Carsten Riether, Ramin Radpour, Nils M. Kallen, Damian T. Bürgin, Chantal Bachmann, Christian M. Schürch, Ursina Lüthi, Miroslav Arambasic, Sven Hoppe, Christoph E. Albers, Gabriela M. Baerlocher, and Adrian F. Ochsenbein. Metoclopramide treatment blocks cd93-signaling-mediated self-renewal of chronic myeloid leukemia stem cells. *Cell Reports*, 34:108663, 1 2021. ISSN 2211-1247. doi: 10.1016/J.CELREP.2020.108663.

N. Joan Abbott, Lars Rönnbäck, and Elisabeth Hansson. Astrocyte–endothelial interactions at the blood–brain barrier. *Nature Reviews Neuroscience 2006 7:1*, 7:41–53, 1 2006b. ISSN 1471-0048. doi: 10.1038/nrn1824.

9 Appendix

9.1 Amplification plots

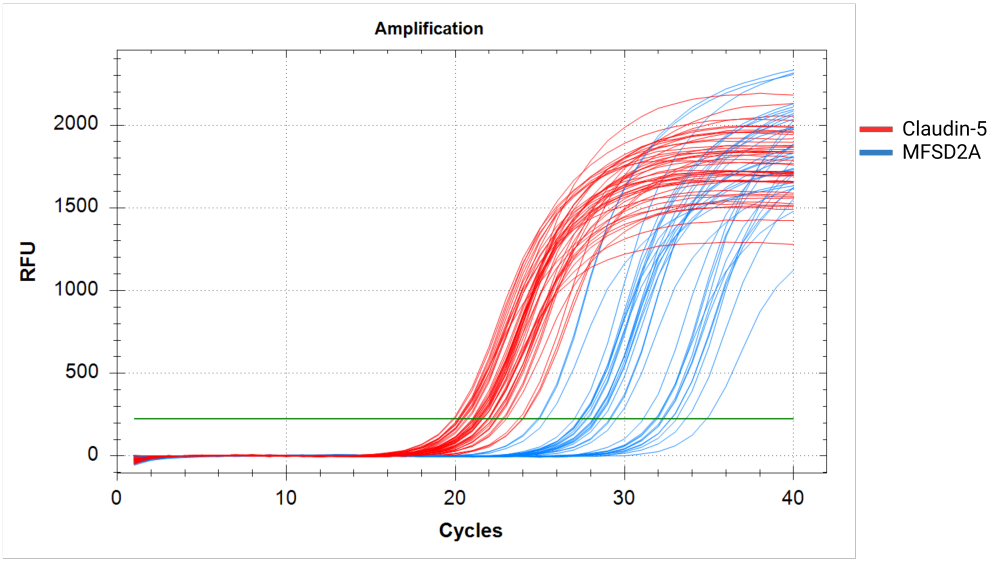

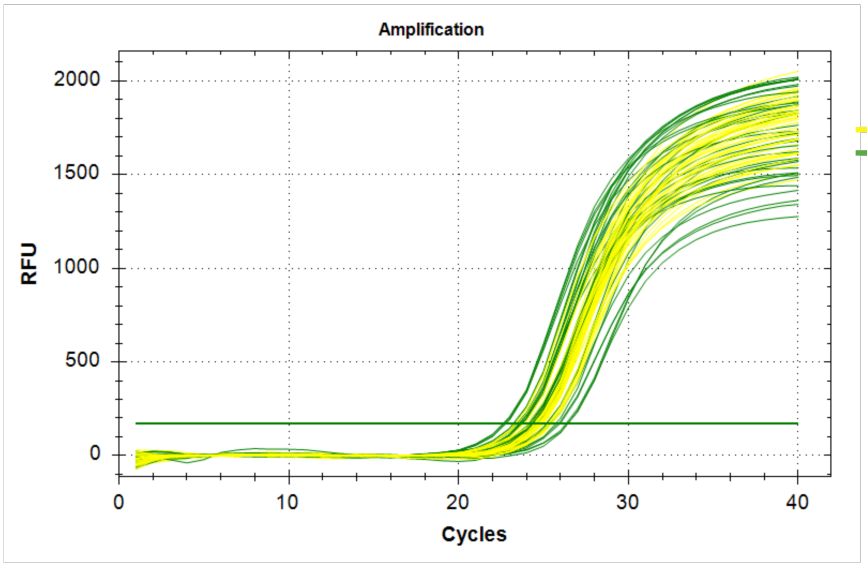
Amplification
RFU
2000
1500
1000
500
0
0
10
20
30
40
Cycles
ZO-1
CD93

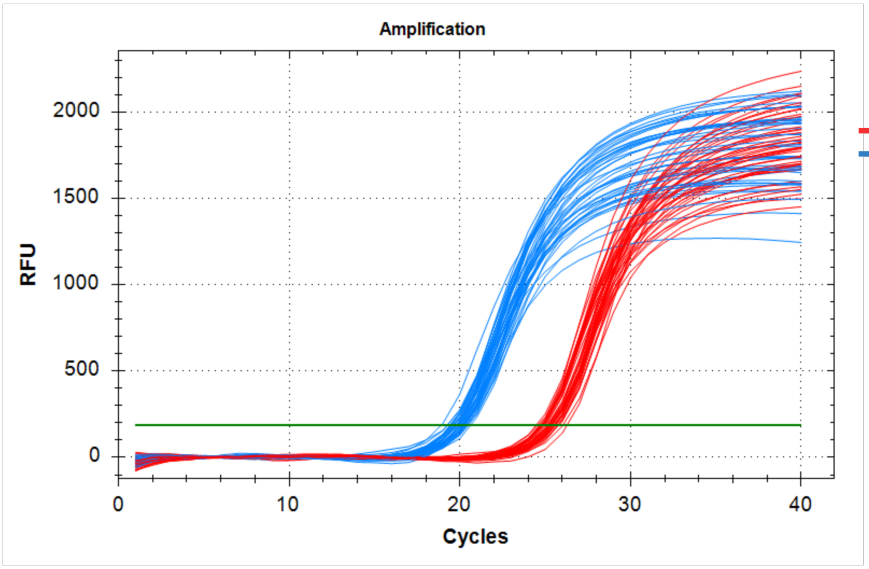
Amplification
RFU
2000
1500
1000
500
0
0
10
20
30
40
Cycles
HPRT1
GAPDH

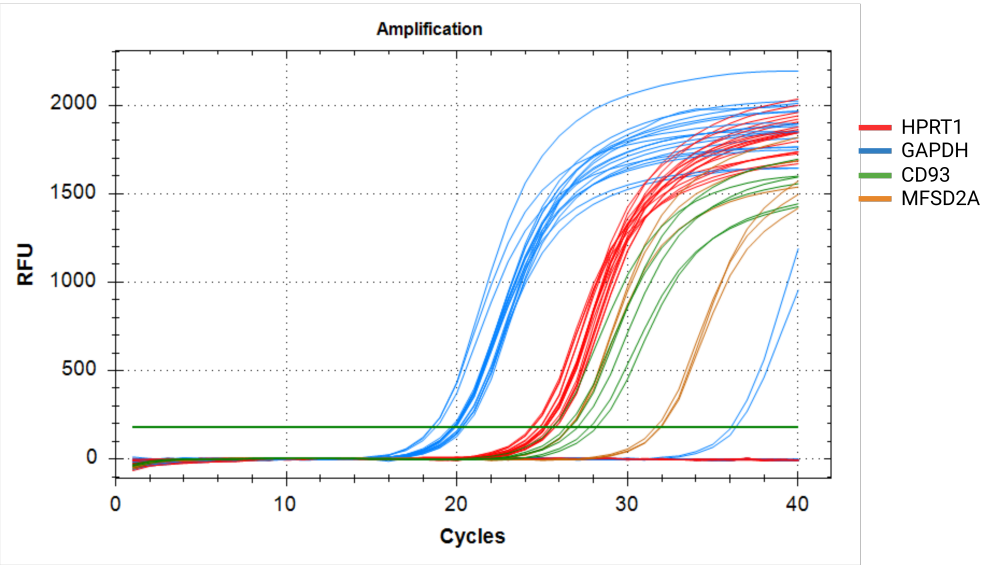
Amplification
RFU
2000
1500
1000
500
0
0
10
20
30
40
Cycles
HPRT1
GAPDH
CD93
MFSD2A

9.2 Melting Point plots

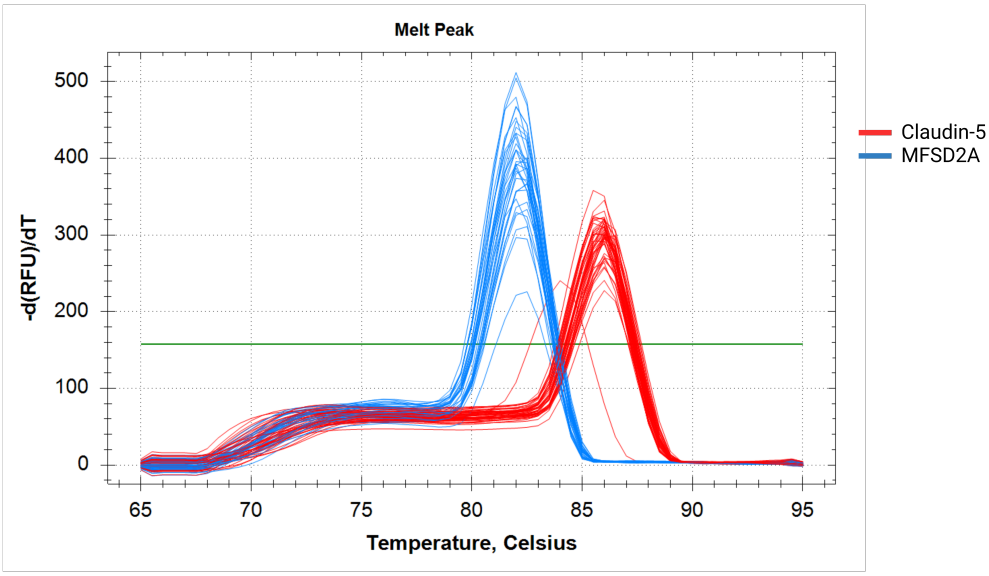

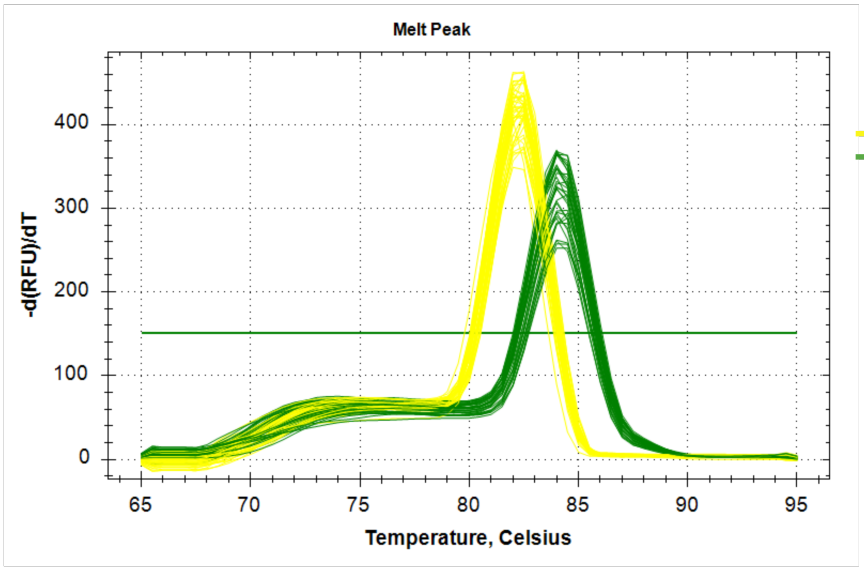
Melt Peak
-d(RFU)/dT
400
300
200
100
0
65
70
75
80
85
90
95
Temperature, Celsius
ZO-1
CD93

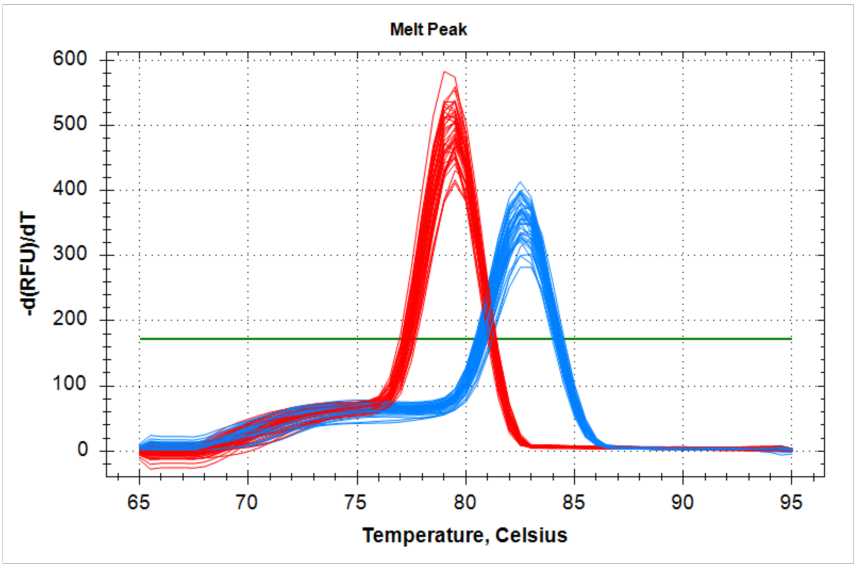
Melt Peak
-d(RFU)/dT
600
500
400
300
200
100
0
65
70
75
80
85
90
95
Temperature, Celsius
HPRT1
GAPDH

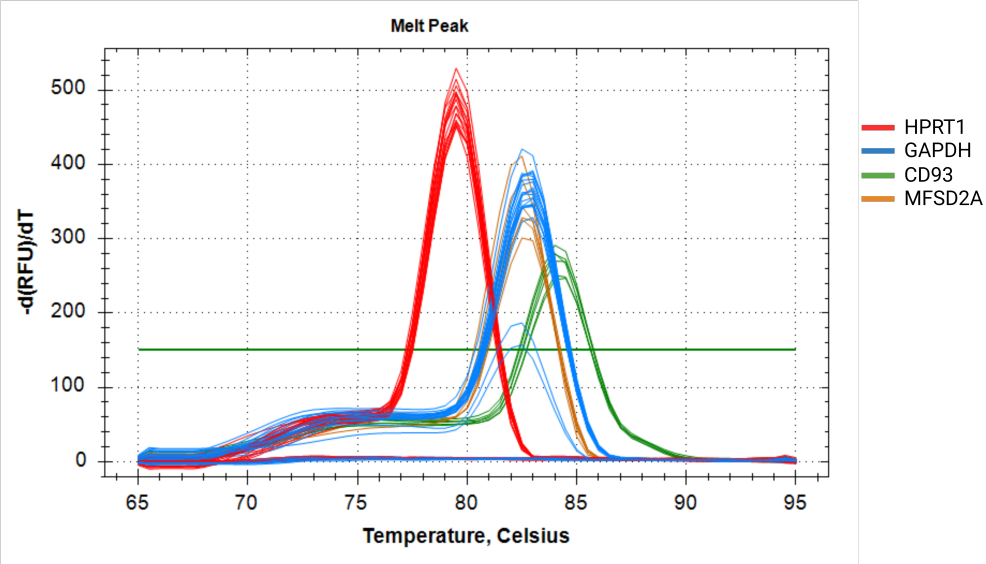
Melt Peak
-d(RFU)/dT
500
400
300
200
100
0
65
70
75
80
85
90
95
Temperature, Celsius
HPRT1
GAPDH
CD93
MFSD2A